

This is a revised version of a manuscript submitted for publication in JAMES. Please note that the manuscript is currently under review and has yet to be formally accepted for publication. Subsequent versions of this manuscript may have slightly different content. If accepted, the final version of this manuscript will be available via the 'Peer-reviewed Publication DOI' link.

---

## **Eddy-mean flow interaction with a Multiple Scale Quasi Geostrophic model**

Bruno Deremble, CNRS ([bruno.deremble@cnrs.fr](mailto:bruno.deremble@cnrs.fr))

Takaya Uchida, FSU ([tuchida@fsu.edu](mailto:tuchida@fsu.edu))

William K. Dewar, FSU ([wdewar@fsu.edu](mailto:wdewar@fsu.edu))

Roger M. Samelson, OSU ([roger.samelson@oregonstate.edu](mailto:roger.samelson@oregonstate.edu))

# Eddy-mean flow interaction with a Multiple Scale Quasi Geostrophic model

Bruno Deremble<sup>1</sup>, Takaya Uchida<sup>1,2</sup>, William K. Dewar<sup>1,3</sup>, Roger M. Samelson<sup>4</sup>

<sup>1</sup>Université Grenoble Alpes, CNRS, INRAE, IRD, Grenoble-INP, Institut des Géosciences de l'Environnement, Grenoble, France

<sup>2</sup>Center for Ocean Atmospheric Prediction Studies, Florida State University, Tallahassee, FL, USA

<sup>3</sup>Dept. of Earth, Ocean, and Atmospheric Science, Florida State University, Tallahassee, FL, USA

<sup>4</sup>College of Earth, Ocean, and Atmospheric Sciences, Oregon State University, OR, USA

## Key Points:

- We implement a numerical version of a Multiple Scale Quasi-Geostrophic model.
- Multiple Scale Quasi Geostrophy allows for variable stratification and variable Coriolis parameter.
- The Multiple Scale Quasi-Geostrophic model reproduces the dynamics of a high resolution primitive equation model.

---

Corresponding author: Bruno Deremble, [bruno.deremble@cnrs.fr](mailto:bruno.deremble@cnrs.fr)

**Abstract**

Parameterization of mesoscale eddies in coarse resolution ocean models are necessary to include the effect of eddies on the large-scale oceanic circulation. We propose to use a multiple-scale quasi-geostrophic model to capture the eddy dynamics that develop in response to a prescribe large-scale flow. The multiple scale quasi geostrophic model consists in extending the traditional quasi-geostrophic dynamics to include the effects of a variable Coriolis parameter and variable background stratification. Solutions to this multiple-scale quasi-geostrophic equation are computed numerically and compared to a full primitive equation model. The large-scale flow field permits baroclinically unstable quasi-geostrophic waves to grow. These instabilities saturate due to nonlinearities and a filtering method is applied to remove large-scale structures that develop due to the upscale cascade. The resulting eddy field represents a dynamically consistent response to the prescribed background flow, and can be used to rectify the large-scale dynamics. Comparisons between Gent-McWilliams eddy parameterization and the present solutions show large regions of agreement, while also indicating areas where the eddies feed back onto the large scale in a manner that the Gent-McWilliams parameterization cannot capture. Also of interest is the time variability of the eddy feedback which can be used to build stochastic eddy parameterizations.

**Plain Language Summary**

Climate models are running at horizontal spatial resolutions that capture only the basin-scale dynamics. This is a strong limitation because the missing mesoscale eddies have a non-negligible impact on the large-scale flow. The problem of including the effect of eddies in climate models is a long standing issue in the ocean modeling community. In this work, we decompose the ocean dynamics into stationary large-scale dynamics and turbulent small-scale dynamics. One can thus write a system of equations for the large-scale dynamics – which can be interpreted as the ocean dynamics given by climate models – and another system of equations for the small-scale dynamics. The numerical implementation of this model reveals that this reduced system of equations faithfully reproduces the dynamics of a high resolution ocean model. This paper is a first step that will eventually guide us to use this model as a parameterization of unresolved scales in low resolution ocean models.

**1 Introduction**

Parameterization of mesoscale eddies in coarse resolution models is a long standing issue in oceanography because while eddies have a disproportionately large impact on the global trans-

46 port of heat and tracers (Griffies et al., 2015; Gnanadesikan et al., 2015), we often lack the com-  
47 putational resources to accurately resolve them. As of today, it is still not clear how small-scale  
48 eddies affect the large-scale oceanic circulation nor how their effects should be parameterized.

49 Gent & McWilliams (1990, henceforth denoted GM) accomplished a major breakthrough  
50 to build such a parameterization when they proposed a first order closure scheme that mimics the  
51 role of the eddies based on the large-scale stratification only. This parameterization has been dis-  
52 cussed and enhanced (Griffies, 1998; McDougall & McIntosh, 2001; Meunier et al., 2023), and  
53 is now routinely used in ocean models (Gent, 2011). The idea behind this parameterization is that  
54 ocean eddies restore slanted isopycnal surfaces to a level state of rest in an adiabatic way. In terms  
55 of energy transfer, this corresponds to a situation where eddies tap into the large-scale potential  
56 energy reservoir and have thus a tendency to flatten isopycnal surfaces.

57 Since the seminal work of Gent & McWilliams (1990), there has been several attempts to  
58 augment the formulation of the parameterization of mesoscale eddies. For instance, Visbeck et  
59 al. (1997) and Treguier et al. (1997) have proposed to adjust the magnitude of the rectification  
60 based on a stability criteria of the large-scale flow. Cessi (2008) and Eden & Greatbatch (2008),  
61 on the other hand, try to constrain the rectification based on the eddy energetics. It is also a well  
62 know issue that the rectification is sensitive to how the adiabaticity is relaxed near the surface  
63 and bottom boundaries (e.g. Ferrari et al., 2008; Ferrari et al., 2010; Uchida, 2019, his Appendix D).  
64 A synthesis of the different approaches appears in (Gent, 2011, and references therein). More re-  
65 cently Marshall et al. (2012) have proposed a GEOMETRIC approach for which the amplitude  
66 of the rectification scales with the eddy geometry and energy – dynamical variables that char-  
67 acterize the unresolved eddy activity – and has shown some success (Mak et al., 2017, 2022). In-  
68 spired by all these developments, we propose the hypothesis that there exists an alternative to the  
69 GM parameterization in the form of a dynamical model of intermediate complexity. To test this  
70 hypothesis, we will use the numerical version of the multiple scale quasi geostrophic model orig-  
71 inally derived by Pedlosky (1984) and confirmed and expanded by Grooms et al. (2011). The deriva-  
72 tion of this multiple scale model relies on the principle of scale separation between the large-scale  
73 dynamics and the small-scale turbulent flow. With this separation of scales, one can decompose  
74 the Navier-Stokes equations into two sets of equations: an equation set for the large-scale Plan-  
75 etary geostrophic (PG) dynamics and one equation set for the small-scale Quasi-Geostrophic (QG)  
76 dynamics. The QG model derived in this framework of multiple scale formalism is richer than  
77 the traditional QG equations because the background stratification and the Coriolis parameters  
78 are functions of space (and thus, the deformation radius is no longer restricted to be spatially uni-

79 form; Theiss, 2006). Eddies generated in this framework will then feel the slow variations of the  
80 large-scale structure of the thermocline.

81 Smith (2007), Killworth & Blundell (2007) and Tulloch et al. (2011) have worked on the  
82 linear version of this model in a realistic context: they computed the characteristic length scales  
83 and time scales of the baroclinic instability and showed that there is a good agreement between  
84 the observed eddy length scale and the instability length scale. Following the same idea, Venaille  
85 et al. (2011) proposed a non-linear implementation of this multiple scale model: from an ocean  
86 general circulation model they extracted vertical hydrographic and velocity profiles in several lo-  
87 cations in the Antarctic circumpolar current and used these profiles to force several doubly pe-  
88 riodic quasi-geostrophic models at all these locations. They showed that each QG model is ca-  
89 pable of reproducing some oceanic structures such as rings or jets and they found a good corre-  
90 spondence between the structure of the flow in each QG module and in a primitive equation (PE)  
91 simulation; although with an offset in the energy levels.

92 We will use a relatively similar setup as Venaille et al. (2011) except that we will deploy  
93 the multiple scale QG (MSQG) equation at the basin scale. To our knowledge, this is the first time  
94 such a model is implemented at the basin scale. In order to validate the model, we will first con-  
95 struct a reference high resolution primitive equation configuration of an extra-tropical ocean basin.  
96 In this configuration, we will diagnose the mean flow and eddy dynamics. This run will serve  
97 as a reference configuration. We will then run the MSQG model with the background flow of the  
98 reference run: we will then compare the eddy statistics of the full model and the reduced model.  
99 For a given mean flow, we will study how the eddies organize to feedback onto the large-scale  
100 solution. This approach is richer than the GM parameterization for at least three reasons. First,  
101 the GM parameterization is meant to flatten isopycnal surfaces everywhere (no matter the type  
102 of oceanic dynamics). This property is based on the dynamics we expect from baroclinic insta-  
103 bility and is probably a very good approximation in most places of the ocean. However, we know  
104 that eddies have sometimes the tendency to steepen isopycnal slopes, especially near jets (Shevchenko  
105 & Berloff, 2015; Porta Mana & Zanna, 2014; Waterman & Jayne, 2011). In such places, first or-  
106 der parameterizations may misrepresent ocean dynamics. Another reason is that by design, first  
107 order closure use a locality hypothesis: eddies are generated and interact with the mean flow at  
108 the same location. However, with the MSQG model, eddies are explicitly represented and they  
109 are free to propagate in and out of regions of high and low baroclinicity. Thus, we expect that the  
110 inverse cascade will be effective beyond the local region of eddy production. And the last rea-  
111 son is that first order closures predict a stationary response for a given mean flow. The commu-

112 nity has been aware of this issue for several years and there has been several propositions to build  
 113 a non stationary rectification of the large-scale flow mostly in the form of energy backscattering  
 114 where one reinjects the sub-grid (unresolved) energy back into the resolved flow as eddies would  
 115 rectify the large-scale flow if resolved (e.g. Jansen et al., 2019; Bachman, 2019; Juricke et al., 2019;  
 116 Uchida et al., 2022, and references therein) and/or stochastic parameterizations (M emin, 2014;  
 117 Porta Mana & Zanna, 2014; Grooms, 2016; Li et al., 2023; Ryzhov et al., 2020; Guillaumin &  
 118 Zanna, 2021). Our approach provides a natural way to handle this issue of non-stationary response  
 119 and we will see how our implementation can actually be used to guide stochastic parameteriza-  
 120 tions.

121 The plan of the paper is as follows. In section 2, we describe the MSQG equation and we  
 122 discuss the link between the inverse cascade in QG and the GM parameterization. In section 3,  
 123 we set up a high resolution primitive equation model that will serve as a reference case. In this  
 124 section, we also compare the dynamics of the MSQG model when forced by the mean flow of  
 125 the eddy resolving model. In section 4, we analyze how eddies modify the large-scale PV, and  
 126 the large-scale buoyancy. We also discuss how these results can be used as a substitute to the GM  
 127 parameterization.

## 128 **2 Model and methods**

### 129 **2.1 Primitive equations in the general case**

130 The generic hydrostatic Boussinesq primitive equations in the oceanic context are

$$\frac{\partial \tilde{\mathbf{u}}_h}{\partial t} + \tilde{\mathbf{u}} \cdot \nabla \tilde{\mathbf{u}}_h + f \mathbf{k} \times \tilde{\mathbf{u}}_h = -\nabla_h P + \mathcal{T} + \mathcal{D}_u \quad (1a)$$

$$\frac{\partial \tilde{b}}{\partial t} + \tilde{\mathbf{u}} \cdot \nabla \tilde{b} = Q + \mathcal{D}_b + \mathcal{R} \quad (1b)$$

$$\frac{\partial P}{\partial z} = \tilde{b} \quad (1c)$$

$$\nabla \cdot \tilde{\mathbf{u}} = 0, \quad (1d)$$

131 with the buoyancy  $\tilde{b}$ , the velocity  $\tilde{\mathbf{u}}$  (and the subscript  $h$  is for the horizontal component). Note  
 132 that we write all primitive equation variables with a tilde ( $\tilde{\mathbf{u}}, \tilde{b}$ ) to not confuse these variables with  
 133 the quasi-geostrophic variables that we will introduce soon.  $P$  is the dynamical pressure (pres-  
 134 sure divided by a constant density in the Boussinesq framework),  $f$  the Coriolis parameter and  
 135  $\mathbf{k}$  is the unit vertical vector.  $\mathcal{T}$  is the wind stress forcing at the surface only and  $\mathcal{D}_u$  is a dissipa-

136 tive term: bi-harmonic viscosity plus linear bottom friction for the velocity field just above the  
 137 sea floor. For simplicity we use a linear equation of state

$$\underline{b} = g\alpha\theta, \quad (2)$$

138 with  $\theta$  the potential temperature,  $\alpha$  the thermal expansion coefficient, and  $g$  the acceleration due  
 139 to gravity. In the rhs of Eq. (1b) we have, a forcing term  $\underline{Q}$  which will be a relaxation towards  
 140 a prescribed temperature profile (to mimic the combination of solar heat flux and air-sea heat fluxes  
 141 with no seasonal variations). In the buoyancy equation, there is also a dissipation term  $\mathcal{D}_b = -A_4\nabla^4\underline{b} +$   
 142  $A_z\partial^2\underline{b}/\partial z^2$ ; with  $A_4$ , and  $A_z$  the constant horizontal and vertical diffusivity coefficients respec-  
 143 tively.

144 The last term in Eq. (1b),  $\mathcal{R}$  corresponds to the effect of small-scale eddies on the large-  
 145 scale flow which is traditionally included only in coarse resolution models. We recall the main  
 146 properties of this term in the next subsection. We also introduce the Reynolds decomposition

$$X = \overline{X} + X', \quad (3)$$

147 with the overbar the ensemble averaging operator and  $X'$  the deviation from the mean. Because  
 148 in this study we will use a stationary forcing, we can reinterpret the ensemble averaging as a time  
 149 averaging. Also, we use “large-scale flow”, “mean flow”, or background flow to designate the  
 150 ensemble mean. And we use “small-scale flow” or “eddy flow” to designate the deviation with  
 151 respect to the mean.

## 152 2.2 Quasi geostrophic model for the eddy flow

153 To model the evolution of the eddy flow, we deploy a multiple scale quasi geostrophic model.  
 154 In the multiple scale formalism originally derived by Pedlosky (1984) (see also Grooms et al.,  
 155 2011; Jamet et al., 2021), the small-scale dynamics are governed by the quasi-geostrophic equa-  
 156 tion which is forced solely by the large-scale flow. The traditional quasi-geostrophic equations  
 157 with only one dynamical variable is known to faithfully reproduce mesoscale eddies with a small  
 158 number of levels in the vertical discretization. The QG model is thus a good candidate for a model  
 159 of intermediate complexity (compared to the primitive equation model) that still exhibits real-  
 160 istic eddy dynamics. In this system of equation, the main variable is the quasi-geostrophic po-  
 161 tential vorticity (PV)

$$q = \nabla^2 \psi + \Gamma \psi, \quad (4)$$

162 with  $\psi$  the small-scale stream function and  $\Gamma$  is the vertical stretching operator

$$\Gamma \psi = \frac{\partial}{\partial z} \left( \frac{f^2}{N^2} \frac{\partial \psi}{\partial z} \right) = \frac{\partial}{\partial z} \frac{f}{N^2} b, \quad (5)$$

163 with

$$b = f \frac{\partial \psi}{\partial z}, \quad (6)$$

164 the small-scale buoyancy, and

$$N^2 = \frac{\partial B}{\partial z}, \quad (7)$$

165 the Brunt-Vaisala frequency squared;  $B$  being the prescribed background buoyancy. Note that in  
 166 order not to confuse the background variables (which are prescribed) and the averaged variables  
 167 of the eddy flow (noted with an overbar), we write all background variables with a capital letter.

168 The QG model is posed theoretically in the continuously stratified setting, for consistency  
 169 with the primitive-equation formulation, but only a small number of levels, or equivalent local  
 170 vertical modes, are required to represent the dominant mesoscale eddy fluxes, because of the small  
 171 length scales of the higher modes. This vertically-discretized QG model can be physically inter-  
 172 preted as an equivalent layer model (see Section 3.2 and Appendix B). The numerical implemen-  
 173 tation nonetheless uses a 3D elliptic solver with  $\psi = 0$  on the lateral boundaries (no-normal-flow),  
 174 and  $\partial \psi / \partial z = 0$  at the upper and lower boundaries (zero buoyancy anomaly), which gives a 3D  
 175 solution for  $\psi$  that is consistent with the layer-model interpretation. Note that the top and bot-  
 176 tom boundary conditions correspond to the standard assumption in QG that buoyancy vanishes  
 177 at the top and bottom surfaces. As we shall see henceforth, this condition is very helpful in the  
 178 context of eddy parameterization (see discussion in the next section). In the general case, it is of  
 179 course possible to adopt a ‘‘surface QG’’ boundary condition where the top and bottom buoyancy  
 180 become a dynamical variable (a strategy that we did not adopt here; see e.g. Roulet et al., 2012).

181 The key point of the multiple scale quasi geostrophic (MSQG) model is that the Coriolis  
 182 parameter and the background buoyancy frequency can both vary slowly in space (Pedlosky, 1984).  
 183 This is actually a major difference compared to the traditional definition of QG PV where  $f$  and  
 184  $N^2$  are constants in the stretching operator (Vallis, 2017). Although richer than traditional QG,

185 we anticipate that with such WKB assumption that  $f$  and  $N^2$  are slow functions of space, the MSQG  
 186 model will not conserve energy and enstrophy (see Appendix B). The equation of evolution of  
 187 QG PV is

$$\frac{\partial q}{\partial t} + \mathbf{u} \cdot \nabla q + \mathbf{U} \cdot \nabla q + \mathbf{u} \cdot \bar{\nabla} Q = \mathcal{D}_q - \mathcal{F}_q, \quad (8)$$

188 with  $\mathbf{u}$  the small-scale velocity field

$$\mathbf{u} = \left( -\frac{\partial \psi}{\partial y}, \frac{\partial \psi}{\partial x} \right). \quad (9)$$

189 and with  $\mathbf{U}$  the rotational component of the background flow

$$\mathbf{U} = (U, V) = \left( -\frac{\partial \Psi}{\partial y}, \frac{\partial \Psi}{\partial x} \right). \quad (10)$$

190 with  $\Psi$  the background stream function. In the multiple scale QG formalism, the background PV  
 191 is

$$Q = f + \Gamma \Psi, \quad (11)$$

192 and the gradient of the large-scale vorticity is

$$\bar{\nabla} Q = (\Gamma V, \beta - \Gamma U). \quad (12)$$

193 where the operator  $\bar{\nabla}$  is written with an overbar to emphasize the multiple scale formalism (see  
 194 Appendix B). The dissipative effects and bottom friction are written as

$$\mathcal{D}_q = A_2 \nabla^2 q - A_4 \nabla^4 q - r \nabla^2 \psi, \quad (13)$$

195 with  $A_2$  and  $A_4$  the harmonic and bi-harmonic dissipation coefficients, and  $r$  the bottom friction  
 196 coefficient (non zero at the bottom only). The harmonic and bi-harmonic operators act on the total  
 197 PV: in the primitive equation, that would correspond to the combined effect of a viscous operator  
 198 acting on the velocity field and a diffusivity operator on the buoyancy with the same viscous  
 199 and diffusivity coefficients. Last,  $\mathcal{F}_q$  is a filtering term to ensure that  $q$  remains a small-scale  
 200 variable. It is in fact a parameterization of the term  $\overline{\nabla \cdot \mathbf{u} q}$  which formally appears in the deriva-  
 201 tion as a higher order term in the multiple-scale expansion (Grooms et al., 2011). In a similar con-

202 text, Uchida et al. (2022) parameterized this term as a damping of the large-scale component of  
 203  $q$ :

$$\mathcal{F}_q = \frac{\widehat{q}}{\tau_f}, \quad (14)$$

204 where  $\widehat{q}$  is the low pass filtered PV and  $\tau_f$  a relaxation time scale (which should be a fast time  
 205 scale compared to the ventilated thermocline time scale; see also Appendix A1). We implemented  
 206 this model with the basilisk framework (<http://basilisk.fr>). It is freely available (see Open  
 207 Research Section) and we provide more details on the numerical recipes in Appendix B.

### 208 **2.3 GM parameterization**

209 We now turn our attention to the strategy to couple a low resolution implementation of Eqs. (1)  
 210 with a high resolution MSQG model. The term  $\mathcal{R}$  in Eq. (1b) represents the effect of the small-  
 211 scale eddies on the large-scale flow and is usually active only for coarse resolution models. For-  
 212 mally this term is meant to represent the unresolved eddy-eddy interaction: from a straightfor-  
 213 ward Reynolds decomposition, one gets

$$\mathcal{R} = -\nabla \cdot \overline{\mathbf{u}'\mathbf{b}'}, \quad (15)$$

214 We decompose the eddy flux  $\overline{\mathbf{u}'\mathbf{b}'}$  into a diapycnal and an isopycnal flux and neglect the diapy-  
 215 cnal flux (to mimic the effect of baroclinic instability). A convenient way to write this term is to  
 216 formulate it as an advection of the ensemble averaged buoyancy by the eddy induced velocity

$$\mathcal{R} = -\mathbf{u}^* \cdot \nabla \overline{b}, \quad (16)$$

217 with

$$\mathbf{u}^* = -\nabla \times \frac{\overline{\mathbf{u}'\mathbf{b}' \times \nabla \overline{b}}}{|\nabla \overline{b}|^2}, \quad (17)$$

218 the non divergent eddy induced velocity, if we only retain the isopycnal component of the eddy  
 219 flux (Zhao & Vallis, 2008). If we further neglect the horizontal gradient of buoyancy compared  
 220 to the vertical gradient of buoyancy, we get

$$\mathbf{u}^* = (\partial_z \Upsilon, -\nabla_h \cdot \Upsilon), \quad (18)$$

221 with  $\mathbf{\Upsilon} = (\Upsilon^x, \Upsilon^y)$ , the eddy-induced transport (see Ferrari et al., 2010)

$$\mathbf{\Upsilon} = -\frac{\overline{u'_h b'}}{N^2}. \quad (19)$$

222 Gent & McWilliams (1990) proposed a parameterization of this eddy induced transport in  
 223 the form of

$$\mathbf{\Upsilon}^{\text{GM}} = \kappa \frac{\nabla \overline{b}}{N^2} \quad (20)$$

224 with  $\kappa$  an eddy induced diffusion coefficient.

225 One goal of our analysis is to propose an alternative form to the GM parameterization by  
 226 explicitly computing the eddy induced transport as in Eq. (19).

#### 227 **2.4 Eddy induced transport in the QG model**

228 With the MSQG model, one can indeed compute  $\overline{ub}$  (with  $u$  and  $b$  now QG variables) which  
 229 can then be used to compute the eddy induced transport as

$$\mathbf{\Upsilon} = -\frac{\overline{ub}}{N^2}. \quad (21)$$

230 For a small number of vertical levels in the QG implementation, the eddy induced trans-  
 231 port will only capture the low baroclinic modes dynamics which is what modern GM parame-  
 232 terizations are actually aiming at (Ferrari et al., 2010). Note also that the eddy induced transport  
 233  $\mathbf{\Upsilon}$  vanishes at the lower and upper boundaries (because  $b = 0$  by construction in the QG model)  
 234 such that there is no transport across these boundaries (as required). Once we know the eddy in-  
 235 duced transport, we can compute the eddy induced velocity that we can then use to compute  $\mathcal{R}$   
 236 in the coarse resolution model.

237 An alternative approach is to compute  $\mathcal{R}$  directly as

$$\mathcal{R} = -\nabla \cdot \overline{ub}, \quad (22)$$

238 such that we skip the step to compute the eddy induced transport. For this approach, we can ei-  
 239 ther directly compute  $\nabla \cdot \overline{ub}$ , or we can use the filtering term in Eq. (8). Let us elaborate the lat-  
 240 ter approach: we first note that in a statistically steady state, time averaging Eq. (8) results in

$$\overline{\mathcal{F}_q} = -\nabla \cdot \overline{\mathbf{u}q}. \quad (23)$$

241 One can convert this PV forcing term  $\overline{\mathcal{F}_q}$  into a stream function forcing via Eq. (4)

$$\overline{\mathcal{F}_q} = \nabla^2 \overline{\mathcal{F}_\psi} + \Gamma \overline{\mathcal{F}_\psi} \simeq \Gamma \overline{\mathcal{F}_\psi}, \quad (24)$$

242 where  $\overline{\mathcal{F}_\psi}$  is the large-scale stream function forcing. Hence, if we know  $\overline{\mathcal{F}_q}$ , we can compute  $\overline{\mathcal{F}_\psi}$   
 243 by solving the elliptic equation (24). Note that since  $\overline{\mathcal{F}_q}$  and  $\overline{\mathcal{F}_\psi}$  are large-scale fields, the hor-  
 244 izontal Laplace operator in Eq. (24) is negligible compared to the vertical stretching term as ex-  
 245 pected from the scale separation. And last, once we know  $\overline{\mathcal{F}_\psi}$ , we can compute the large-scale  
 246 buoyancy forcing (see Eq. (6)).

$$\overline{\mathcal{F}_b} = f \frac{\partial}{\partial z} \overline{\mathcal{F}_\psi}, \quad (25)$$

247 This buoyancy forcing corresponds the average effect of eddies on the large-scale buoyancy and  
 248 is precisely the meaning of the term  $\mathcal{R}$  in Eq. (1b)

$$\overline{\mathcal{F}_b} = \mathcal{R} = -\nabla \cdot \overline{\mathbf{u}b}. \quad (26)$$

249 We will compute  $\mathcal{R}$  with both methods in the next section and discuss the pros and cons  
 250 of each strategy.

## 251 **2.5 GM parameterization and PV homogenization**

252 To close this section on the GM parameterization, we note that in the limit of scale sepa-  
 253 ration between the eddy scale and the gyre scale, buoyancy eddy fluxes and PV eddy fluxes are  
 254 related via

$$\overline{\mathbf{u}q} = f \frac{\partial}{\partial z} \frac{\overline{\mathbf{u}b}}{N^2}, \quad (27)$$

255 where the PV flux corresponds in fact to a thickness flux (Treguier et al., 1997) (all variables are  
 256 QG variables). In the GM parameterization, the buoyancy flux is parameterized as a down gra-  
 257 dient flux (see Eq. (19) and Eq. (20)) and can be written in the QG formalism as

$$\overline{\mathbf{u}b} = -\kappa_b \nabla B, \quad (28)$$

258 with  $\kappa_b$  the QG eddy diffusivity coefficient. If we combine Eq. (28) and Eq. (27) and use the def-  
 259 inition of the gradient of large-scale potential vorticity (Eq. (12)), we obtain the QG form of the  
 260 GM parameterization

$$\overline{\mathbf{u}q} = -\kappa \overline{\nabla} Q, \quad (29)$$

261 where we have included the  $\beta$  effect in order to write the gradient of the large-scale PV. This last  
 262 statement is the reason why we have adopted two different notations for the diffusivity coefficient  
 263  $\kappa_b$  in Eq. (28) and  $\kappa$  in Eq. (29) but in the limit where large-scale PV gradients are dominated  
 264 by vortex stretching, we really expect  $\kappa \simeq \kappa_b$ . Equation (29) states that the role of the eddies is  
 265 to homogenize the large-scale PV because when we take the divergence of the rhs of Eq. (29),  
 266 we get a diffusion operator. This property was originally recognized by Rhines & Young (1982)  
 267 in an idealized context. In Rhines and Young's experiment, they had a large-scale baroclinic in-  
 268 put to the PV but the only component to the large-scale PV gradient was  $\beta$ . They did verify that  
 269 in a double gyre configuration, PV was well homogenized in regions of high eddy activity (mostly  
 270 the intergyre) and we can now proceed to a similar verification in a more realistic configuration.

### 271 **3 Application to a mid-latitude basin**

#### 272 **3.1 Reference case with the primitive equation model**

273 Before we focus on the MSQG model, we first construct a full eddy resolving model that  
 274 will serve as a reference case against which we will compare the eddy statistics of the simplified  
 275 model. The configuration of the reference model is directly inspired from Samelson & Vallis (1997),  
 276 although we deploy it in an eddy resolving configuration in a similar way to Grooms & Kleiber  
 277 (2019). With such model, we both capture the large-scale dynamics and the meso-scale eddy dy-  
 278 namics of an extra-tropical basin (idealized version of the North Atlantic ocean). The equations (1)  
 279 are integrated forward in time with the MITgcm (Marshall et al., 1997) in a square domain ( $\beta$ -  
 280 plane) of dimension  $L \times L$ , with  $L = 5000$  km, and maximum depth  $H = 4000$  m away from the  
 281 shelves (see Eq. (32)). We use a uniform horizontal resolution of 5 km (1024 points in each hor-  
 282 izontal direction), and we use a stretched vertical grid of 52 levels with maximum resolution near  
 283 the surface (11 m) and minimum resolution near the bottom (274 m). Note that the horizontal  
 284 resolution of 5 km corresponds to several grid points per deformation radius in most of the do-

285 main but we do not expect to resolve well the turbulence in the northern part of the domain where  
 286 the deformation radius is of the order of 5-10 km. The Coriolis parameter is a function of lati-  
 287 tude  $f = f_0 + \beta(y - y_m)$  with  $f_0$  the mean value of the Coriolis parameter  $f_0 = 8 \times 10^{-5}$ ,  $\beta =$   
 288  $2 \times 10^{-11} \text{ m}^{-1} \text{ s}^{-1}$ , and  $y_m$  the mean latitude.

289 The model is forced at the surface with wind and buoyancy fluxes. The wind stress pro-  
 290 file has a zonal component only

$$\mathcal{T}^x = -\tau_0 \frac{f}{f_0} \sin\left(\frac{2\pi y}{L}\right), \quad (30)$$

291 with  $\tau_0 = 0.08 \text{ N m}^{-2}$ . As in Samelson & Vallis (1997), we choose this wind profile to ensure  
 292 that there is no Ekman flow at the northern and southern boundaries. The buoyancy fluxes are  
 293 a relaxation to a prescribed buoyancy profile with uniform meridional temperature gradient of  
 294 30 K/5000 km. The relaxation time scale is set to

$$T_b = \frac{\rho_0 C_p h_0}{Q} \quad (31)$$

295 with  $\rho_0 = 1000 \text{ kg m}^{-3}$  the constant density of water,  $C_p = 4000 \text{ J kg}^{-1} \text{ K}^{-1}$  the heat capacity  
 296 of water,  $h_0$  the thickness of the upper grid point of the model and  $Q = 35 \text{ W m}^{-2} \text{ K}^{-1}$  a prescribed  
 297 amplitude of the heat flux such that the relation time scale is on the order of 40 days for the up-  
 298 per 30 m of the ocean.

299 Along each meridional and zonal boundary, we use a bathtub-like topography (Salmon, 1994)  
 300 with a shelf given by

$$h_s \exp\left(-\frac{x_n^2}{2d^2}\right), \quad (32)$$

301 with  $x_n$  the coordinate normal to the boundary,  $d = 200 \text{ km}$  the width of the shelf, and  $h_s = 2000 \text{ m}$   
 302 the height of the shelf (with respect to the bottom). This topography drastically affects the dy-  
 303 namics of the western boundary current (Jackson et al., 2006; Stewart et al., 2021): it exerts a con-  
 304 trol on the width of the western boundary current, and on the stability of the separation point.

305 We plot in Fig. 1a the mean stream function  $\Psi$  which corresponds to the rotational part of  
 306 the mean flow and is defined as

$$\nabla^2 \Psi = \frac{\partial \bar{v}}{\partial x} - \frac{\partial \bar{u}}{\partial y} \quad (33)$$

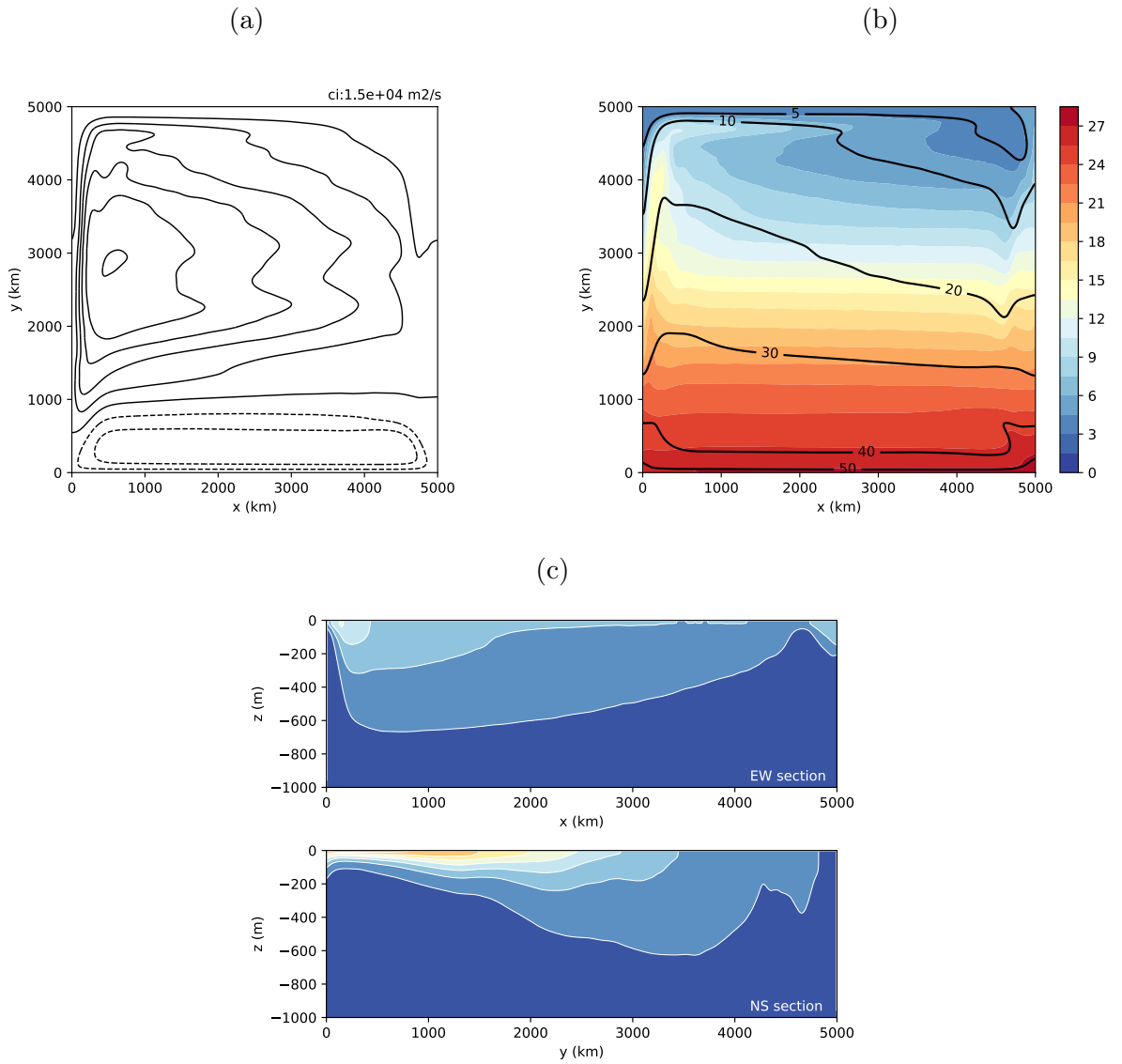


Figure 1: (a): Time mean stream function  $\Psi$  averaged over the upper 172 m. Contour interval is  $1.5 \times 10^4 \text{ m}^2 \text{ s}^{-1}$ . (b): Time mean Sea surface temperature (colors) and first deformation radius (contours, unit: km). (c): Time mean Vertical temperature profiles in the middle of the domain for the upper 1000 m. Top: north-south section. Bottom: east-west section. The colorbar is the same for panels (b) and (c) (unit  $^{\circ}\text{C}$ ).

307 averaged over the upper 172 m and with  $\Psi = 0$  boundary condition on the sides. With the cho-  
 308 sen wind profile, the circulation corresponds to a big anticyclonic gyre (reminiscent of the sub-  
 309 tropical gyre) and one smaller cyclonic gyre near the southern boundary. The flow in the west-  
 310 ern boundary is intensified with a maximum transport of 11 Sv. The strength of this circulation  
 311 decreases with depth (not shown). The corresponding surface temperature field is plotted in Fig. 1b  
 312 (we recall that temperature is linearly related to buoyancy – see Eq. (2)). This temperature map  
 313 exhibits a large-scale north-south gradient, as expected from the atmospheric forcing. A warm  
 314 core western boundary current is present and hugs the topography up to the northern boundary.  
 315 We compute the first deformation radius to emphasize the separation of scale between the eddy  
 316 scale and the gyre scale (Fig. 1b). The deformation radius varies between 50 km near the south-  
 317 ern boundary to 5 km at the northern boundary.

318 Vertical sections of temperature shown in Fig. 1c are taken in the middle of the domain ( $y =$   
 319 2500 km for the zonal section, and  $x = 2500$  km for the meridional section). The thermocline  
 320 which separates the deep ocean from the ventilated layers is visible in the north-south section.  
 321 The depth at which the internal boundary layer is found is set by the wind forcing (Samelson &  
 322 Vallis, 1997). Near  $y = 3000$  km we see a pool of weakly stratified water that is reminiscent of  
 323 the subtropical mode water (Deremble & Dewar, 2013). In this model, it is not clear whether this  
 324 mode water is maintained by a surface buoyancy flux or the Ekman flow convergence at the sur-  
 325 face (Dewar et al., 2005). An unstratified deep ocean is a characteristic feature of closed basin  
 326 models. It is indeed the circumpolar gap that affects the deep stratification (Warren, 1990; Tog-  
 327 gweiler & Samuels, 1995).

328 We plot in Fig. 2 a snapshot of specific eddy kinetic energy defined as

$$EKE = \frac{1}{2}(u'^2 + v'^2), \quad (34)$$

329 and the time mean specific eddy kinetic energy in the upper part of the ocean. As expected, we  
 330 observe an intense eddy activity that is maximum near the western boundary. This maximum of  
 331 EKE follows well the isobath contours and so executes a sharp turn in the north west corner (as  
 332 does the mean flow). There is a relative maximum of EKE near the 4000 km latitude which cor-  
 333 responds approximately to the zero wind stress curl line. Near the northern boundary, there is ev-  
 334 idence of a permanent zonal jet strongly anchored above the topographic shelf (a well known fea-  
 335 ture for  $\beta$ -plane turbulence; see e.g. Simonnet et al., 2021). There is little eddy activity in the south-  
 336 ern part of domain. As we shall see in the next section, most of this eddy activity can be explained

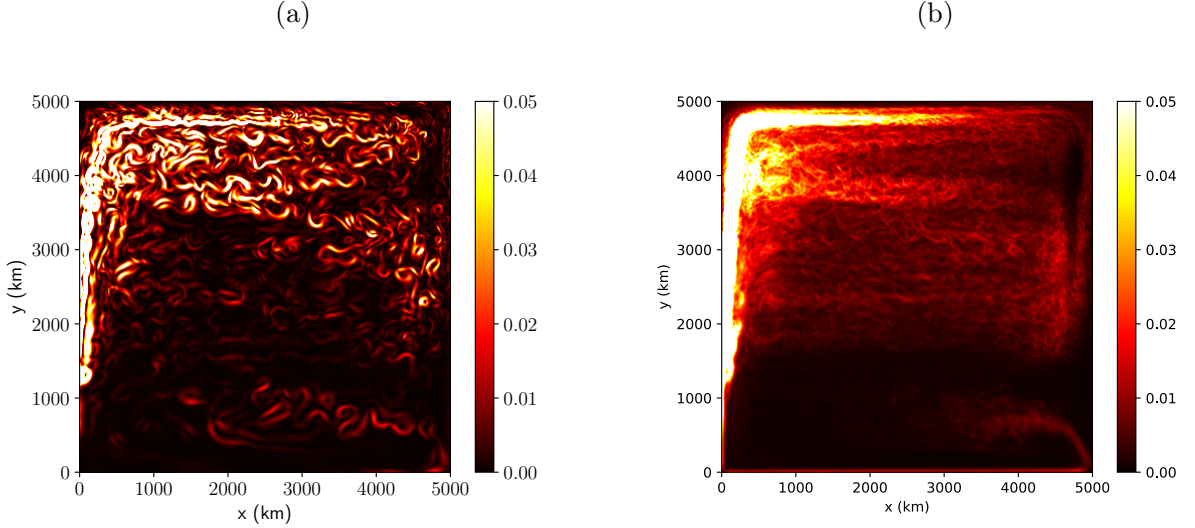


Figure 2: (a): Snapshot of specific eddy kinetic energy (unit:  $\text{m}^2 \text{s}^{-2}$ ). (b): Mean specific eddy kinetic energy (unit:  $\text{m}^2 \text{s}^{-2}$ ). Both fields are averaged over the upper 172 m of the PE model.

337 by the baroclinic instability of the mean flow. Last, in order to examine how the eddies rectify  
 338 the mean flow, we plot both components of the eddy induced transport  $\bar{\mathbf{Y}}$  in Fig. 3. Both Fig. 2  
 339 and Fig. 3 will serve as a reference to which we will compare the QG model. Note that we plot  
 340 the smoothed version where we average  $8 \times 8$  neighboring grid points and linearly interpolate  
 341 back on the fine grid for visualization purposes. All smoothed fields are smoothed this way.

342 This configuration corresponds to the reference case where both the mean flow and the ed-  
 343 dies are well captured by the model. The question we are asking is whether we can take the mean  
 344 flow of this configuration, pretend it comes from a coarse resolution model, and set up a model  
 345 of intermediate complexity that is cheaper to run than the full eddy resolving model, but that can  
 346 still capture the eddy variability and eddy fluxes on the mean flow. To illustrate this approach,  
 347 we use the MSQG model that we described in section 2.2.

### 348 3.2 Results of the MSQG model

349 We integrate the MSQG model (Eq. 8) forward in time starting from rest in the same phys-  
 350 ical domain as the reference model. We use 4 vertical levels of thickness  $h = 172, 359, 936,$  and  
 351  $2531$  m from top to bottom. We recall that  $f_0 = 8 \times 10^{-5}$  and  $\beta = 2 \times 10^{-11} \text{ m}^{-1} \text{ s}^{-1}$  which cor-  
 352 responds to a Rossby number  $Ro = u_s / fl_s$  between 0.015 and 0.067 in the northern and south-  
 353 ern part of the domain respectively (with  $u_s = 0.1 \text{ m s}^{-1}$ , and  $l_s = 50 \text{ km}$ , the characteristic ve-

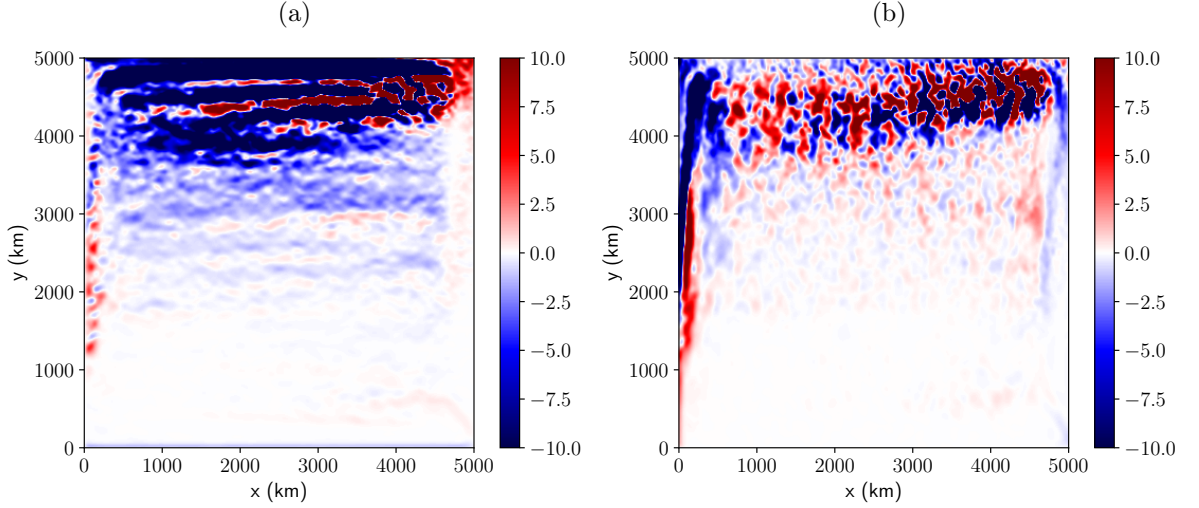


Figure 3: (a) Zonal component, and (b) meridional component of the eddy induced transport  $\Upsilon$ , as defined in Eq. (19) for the PE model averaged in the upper 172 m. Both fields are smoothed by averaging nearby points (see text) (unit:  $\text{m}^2 \text{s}^{-1}$ ).

354 velocity and length scale). We use a bi-harmonic viscosity coefficient  $A_4 = 10^{10} \text{ m}^4 \text{ s}^{-1}$  which cor-  
 355 respond to a bi-harmonic Reynolds coefficient  $Re_4 = 1250$  (with  $Re_4 = u_s l_s^3 / A_4$ ). We set a bot-  
 356 tom drag coefficient with a spin down time scale of  $r^{-1} = 146$  days. This corresponds to an Ek-  
 357 man layer of thickness  $\delta_E = 2r h_l / f_0 = 5 \text{ m}$  (with  $h_l$  the thickness of the bottom layer) or a value  
 358 of the Ekman number  $\delta_E / H = \sqrt{\nu_v / f_0 H^2} = 1.25 \times 10^{-3}$ , which also corresponds to a turbulent  
 359 vertical viscosity in the bottom boundary layer of  $\nu_v = 3 \times 10^{-3} \text{ m}^2 \text{ s}^{-1}$ . The filter  $\mathcal{F}_q$  works ex-  
 360 actly as in Uchida et al. (2022): every 2 days, we proceed to a wavelet decomposition of the stream  
 361 function and we subtract the component of this field that is larger than 550 km (roughly 5 times  
 362 the instability length scale). The total length of the time series is 40 years and the outputs are 30-  
 363 day snapshots. The imposed large-scale stream function  $\Psi$  is computed by solving at each level  
 364 the 2D Poisson equation (Eq. 33) where the time averaged relative vorticity of the PE model is  
 365 vertically coarse grained on the four QG levels (illustration of the upper level stream function is  
 366 given in Fig. 1). With such large-scale stream function, we can compute the large-scale veloc-  
 367 ity  $U$  and  $V$  as shown in Eq. (10). In a similar way, to compute the Brunt-Vaisala frequency  $N^2$ ,  
 368 we first compute the time mean buoyancy field  $B$  of the PE model. We then coarsen this field in  
 369 the vertical dimension on the 4 QG levels. Last, we take the vertical derivative of the latter field  
 370 to get  $N^2$  at the interface between QG levels (in the usual vertical discretization of QG models,  
 371 see Cushman-Roisin & Beckers, 2011).

372 In the first days of the time integration, we first observe a transient phase during which the  
 373 most unstable modes grow. These most unstable modes have a local wavelength that varies in space  
 374 simply because the hydrographic properties of the large-scale flow and the Coriolis parameter  
 375 vary in space. Obviously the time scale of the instability is also a function of space such that all  
 376 parts of the domain do not stay in the transient phase for the same amount of time. As time in-  
 377 creases the amplitude of the linear waves saturate and the system evolves into a fully non-linear  
 378 state. Because we filter the large-scale part of the dynamics, we force the system to stay in an un-  
 379 stable regime that we call a statistically stationary eddying state. With this strategy, we can achieve  
 380 long integrations of the eddy field for a given background flow and we can analyze meaningful  
 381 statistics of eddy fluxes for such mean flow. Henceforth, we only analyze the last 33 years which  
 382 are in statistical steady state.

### 383 3.3 Energetics of the small-scale flow

384 Oceanic eddies carry both kinetic energy defined in the QG formalism as

$$E_k = \frac{1}{2}(u^2 + v^2) = \frac{1}{2}(\nabla\psi)^2 \quad (35)$$

385 and potential energy defined as

$$E_p = \frac{1}{2} \frac{b^2}{N^2} = \frac{1}{2} \frac{f^2}{N^2} \left( \frac{\partial\psi}{\partial z} \right)^2 \quad (36)$$

386 We plot in Fig. 4 snapshot of kinetic energy  $E_k$  and mean kinetic energy  $\overline{E_k}$ . As already  
 387 observed for the reference case, there is a vigorous eddy field, well pronounced in the western  
 388 and northern part of the subtropical gyre. The zones of maximum eddy activity do not necessar-  
 389 ily correspond to the zones of maximum growth rate for the barotropic/baroclinic instability (not  
 390 shown). We recall that the origin of this eddy field is only the baroclinic instability but that ed-  
 391 dies can travel in and out of unstable regions. We recover that there is much more kinetic energy  
 392 in the eddy flow than in the background flow: in the snapshot of  $E_k$  (Fig. 4a), one can see the rings,  
 393 jets, and filaments with maximum velocity on the order of  $1 \text{ m s}^{-1}$  for the most energetic struc-  
 394 tures (whereas the background kinetic energy is much weaker and localized in the western bound-  
 395 ary, not shown). Patterns of potential energy tend to fill the holes of the KE patterns (not shown).  
 396 The plot in Fig. 4 compares well with the reference case both for the snapshot and the mean field.  
 397 We emphasize again that we only have 4 levels in the QG model (compared to the 52 levels in  
 398 the PE model) and only one dynamical variable (compared to 3 in the PE model). We have also

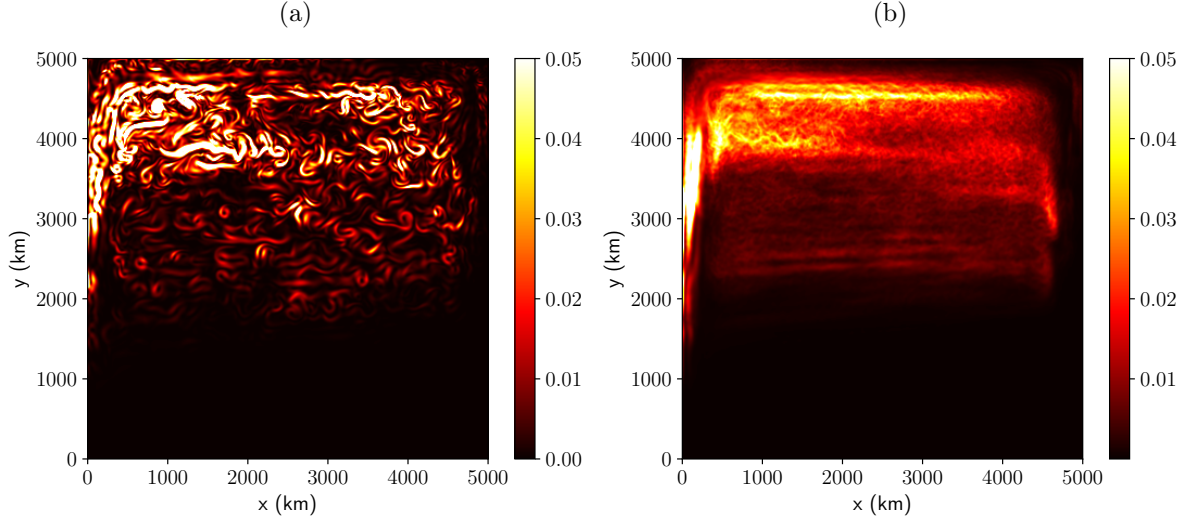


Figure 4: (a) Snapshot of the QG kinetic energy  $E_k$  in the upper level; (b) mean kinetic energy  $\overline{E_k}$  in the upper level. (Same as Fig. 2 but for the QG model)

399 computed the time evolution of the PV field with a traditional QG model (uniform  $N^2$  and uni-  
 400 form  $f$  in the definition of PV – but still with the traditional  $\beta$  effect) and got a poor agreement  
 401 with the reference case (see appendix A).

402 The total kinetic energy in the QG model is 0.2 EJ (1 EJ =  $10^{18}$  J), whereas the total po-  
 403 tential energy is 0.7 EJ. – we have multiplied the kinetic and potential energy in Eq. (35–36) by  
 404 a constant  $\rho_0 = 1000 \text{ kg m}^{-3}$  and integrated over the whole domain to get energies in Joules. So  
 405 we get the same order of magnitude for the kinetic and potential energy which is consistent with  
 406 the QG scaling and the fact that we operate at Burger number close to one. To put these numbers  
 407 in perspective, we can compare these energies with the energy in the large-scale solution: there  
 408 is 22 EJ of available potential energy (APE) and 0.08 EJ of mean kinetic energy which is all con-  
 409 sistent with the energy partition in the ocean (Vallis, 2017). As expected, we have the eddy ki-  
 410 netic energy and eddy potential energy orders of magnitude smaller than the mean APE: there  
 411 is only a small fraction of the large-scale energy reservoir that is drained in the eddy field. We  
 412 also note that the amount of energy contained in the mesoscale field is consistent with the num-  
 413 ber of 13 EJ discussed by Wunsch & Ferrari (2004) for the global eddy energy, given that we study  
 414 only one gyre and that most of the global EKE is in the ACC.

415 To get the energy equation of the small-scale flow, we multiply the equation of evolution  
 416 of PV (Eq. 8) by  $-\psi$  and integrate over the entire domain

$$\frac{\partial E_k + E_p}{\partial t} = \underbrace{\int_{\Omega} (-vUq + uVq) d^3x}_{\text{BI}} - \underbrace{\int_{\Omega} \psi \mathcal{D}_q d^3x}_{\text{SD+BF}} + \underbrace{\int_{\Omega} \psi \mathcal{F}_q d^3x}_{\text{IC}} + \text{res.} \quad (37)$$

417 The three terms in the rhs of (37) are respectively the energy input via baroclinic and barotropic  
 418 instability (BI), the sum of the small-scale dissipation and bottom friction (SD+BF), and the ef-  
 419 fect of the filter that damps large-scale structures that are created via inverse cascade (IC) and are  
 420 the leading order terms in the MSQG model. In the multiple scale formalism, the other terms of  
 421 the energy equation (advection of small-scale energy by the small-scale flow and advection of  
 422 large-scale energy by the small-scale flow) do not exactly vanish in the numerical model and are  
 423 gathered here in the residual term in Eq. (37) (see discussion at the end of this section and Ap-  
 424 pendix B). In a statistical steady state, the leading order balance is between the three terms in the  
 425 rhs of Eq. (37): this corresponds to the classical paradigm where eddies are generated via baro-  
 426 clinic and barotropic instability and energy is dissipated by viscous and diffusive processes plus  
 427 a moderate inverse cascade that is halted by bottom friction. In such a scenario, eddies do not  
 428 feedback on the large-scale flow ( $IC = 0$ ). We show here that, indeed, the eddy feedback on the  
 429 large-scale flow is weak. It is on the same order of magnitude as bottom friction, but this term  
 430 is key to maintain the eddy structure close to the reference run: we also ran the MSQG model  
 431 without the filtering term and we obtained a different eddy field superimposed to a spurious large-  
 432 scale flow (see Appendix A and Uchida et al., 2022).

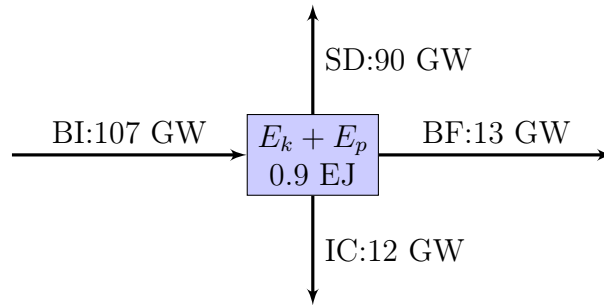


Figure 5: Energy budget of the MSQG model. The unit of the energy reservoir is in EJ (1 EJ =  $10^{18}$  J) and the unit of the energy flux is GW (1 GW =  $10^9$  W). BI stands for baroclinic instability, IC is for inverse cascade, BF is for bottom friction and SD is for small-scale dissipation.

433 We summarize in Fig. 5 the energy budget of the QG model in the configuration that we  
 434 discussed in the previous section. The QG flow finds its energy in the large-scale APE that drives

435 the baroclinic instability. This corresponds to an energy flux of  $BI = 107$  GW. This energy is dis-  
 436 sipated via three mechanism: viscous and diffusive dissipation removes energy at the smallest  
 437 scales ( $SD = 90$  GW), bottom friction dissipates 13 GW and the filter dissipates large-scale struc-  
 438 tures at a rate of 12 GW. For the  $SD$  term, we recall that it is written as a bi-harmonic operator  
 439 acting on both the relative vorticity component and the vortex stretching component. Hence,  $SD$   
 440 corresponds to the sum of a kinetic energy sink and a potential energy sink. The decomposition  
 441 of this term in these two components reveals that 78 GW correspond to a potential energy loss  
 442 whereas 12 GW correspond to a kinetic energy loss. Last, we state again that even if BF and IC  
 443 are weak, they are key processes to maintain a realistic eddy flow. We also note that in a prelim-  
 444 inary work where we used a real planetary geostrophic solution for the large-scale flow (as origi-  
 445 nally derived in Pedlosky, 1984), the IC term was actually the leading order term in the energy  
 446 balance. This is because the planetary geostrophic flow was strongly baroclinically unstable. In  
 447 the planetary geostrophic formalism, we tame these instabilities with friction and viscosity (Colin  
 448 de Verdiere, 1986; Samelson & Vallis, 1997) but if we use this flow as a background state for the  
 449 QG model, then eddies quickly erode the stratification such that the leading order term corresponds  
 450 to this erosion.

451 Finally, we state that the energy budget is not perfectly closed (approximately 7% resid-  
 452 ual). This is an intrinsic property of the multiple scale QG model where  $N^2$  varies in space and  
 453 such that the model does not conserve potential energy. Consider for instance a vortex that car-  
 454 ries both kinetic and potential energy. If the vortex is advected in another location, in the QG for-  
 455 malism, it will conserve its kinetic energy but its potential energy will vary simply because  $N^2$   
 456 varies in space (see Eq. (36)). The only way to minimize this drawback is to use a smooth back-  
 457 ground buoyancy frequency. In the limit where  $N^2$  is constant, then the model conserves both  
 458 kinetic and potential energy (see derivation in Appendix B). From a numerical perspective, we  
 459 were able to close the energy budget (less than 1% residual) when keeping track of all the terms  
 460 that vanish in the traditional QG formalism but do not vanish in the multiple scale formalism (namely  
 461  $\psi \mathbf{u} \cdot \nabla q$  and  $\psi \mathbf{u} \cdot \bar{\nabla} Q$ ).

462 Given that the global energy input by wind to the large-scale circulation is  $O(1$  TW) (Jamet  
 463 et al., 2021), our estimate of dissipation in a single gyre of 100 GW does not seem irrelevant. How-  
 464 ever, any comparison with the real ocean should be taken with a grain of salt for three reasons:  
 465 first, QG dynamics are missing many important phenomena (mixed layer dynamics, unbalanced  
 466 dynamics) that could affect the energy balance. Second, the topography is clearly not realistic  
 467 and the flow-topography interaction is not well represented in QG (Dereble et al., 2017). And

last, the variability of the forcing could trigger a seasonal response in the eddy statistics that is not represented here (see Uchida et al., 2021).

## 4 Rectification term

We now focus on the eddy correlation terms in order to advance toward a parameterization of mesoscale eddies. As a starting point, we analyze the impact of eddies on the mean PV. Then we compute the eddy induced transport and compare this quantity to what was obtained in the reference case. Last, we discuss the variability of the rectification.

### 4.1 Effect on Potential Vorticity

To demonstrate the impact of the eddies on the large-scale PV, we plot in Figure 6  $\nabla \cdot \overline{uq}$  and the average rectification term  $\overline{\mathcal{F}_q}$  taken over a 33 year long time series. We chose the color scale in order to see the patterns of these fields in most of the domain (the colorbar saturates in the northern part of the domain where  $f$  is big and  $N^2$  is small). These two plots should be identical according to Eq. (23), but in fact, the time series of the model is not long enough for the mean to converge. Also, we recall that  $\mathcal{F}_q$  is really a parameterization for  $\nabla \cdot \overline{uq}$  that we approximate with a spatial filter (see Eq. 14) and this parameterization is not perfect as shown in Uchida et al. (2022). Nevertheless, the maxima in these two plots are located at similar geographical locations and the two plots seem to differ from one another by small-scale structures and also near the boundaries. As we approach the boundary we enter a region for which the length scale of the most unstable mode is bigger than the distance to the boundary (not shown). It is clearly a region where we do not expect the filtering strategy to work well. In most of the domain, the balance (Eq. (23)) is helpful because it means we can use either  $\nabla \cdot \overline{uq}$  or  $\overline{\mathcal{F}_q}$  to build a parameterization of mesoscale eddies. In order to estimate the eddy diffusivity  $\kappa$  (see Eq. (29)), we compute the scalar product  $\nabla Q \cdot \overline{uq} / |\nabla Q|^2$  that we plot in Fig. 7. One key result is that the eddy flux of PV is mostly downgradient as illustrated by the fact that this figure is mostly red. Note also that the mean eddy PV flux is dominated by the stretching component. This means that we could have used Eq. (28) to estimate  $\kappa_b$  (the plot of  $\kappa_b$  is actually almost identical to Fig. 7, not shown). In regions where  $\kappa$  is positive, we estimate the magnitude of the eddy diffusivity coefficient to be  $\kappa \sim \mathcal{O}(10^3 - 10^4) \text{ m}^2 \text{ s}^{-1}$ . This is not meant to be an exact number but rather an order of magnitude of the eddy diffusivity. This value is well in the range of values used for eddy diffusivity in low resolution ocean models (Nakamura & Chao, 2000). There are zones with upgradient PV flux near the western boundary (a region of intense eddy activity) and in banded structures in the

499 middle of the domain. The impact of this up-gradient PV flux is to sharpen the large-scale PV  
 500 gradients.

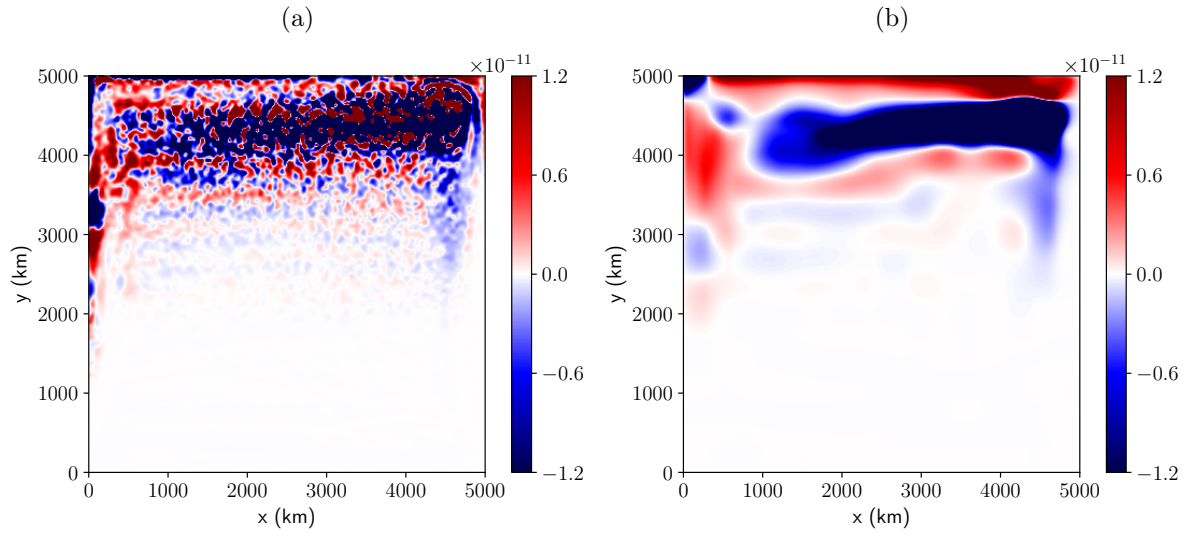


Figure 6: (a):  $-\nabla \cdot \overline{uq}$  (smoothed), (b):  $\overline{\mathcal{F}_q}$  for the MSQG model forced with the mean flow of the PE model. (units are  $s^{-2}$ ).

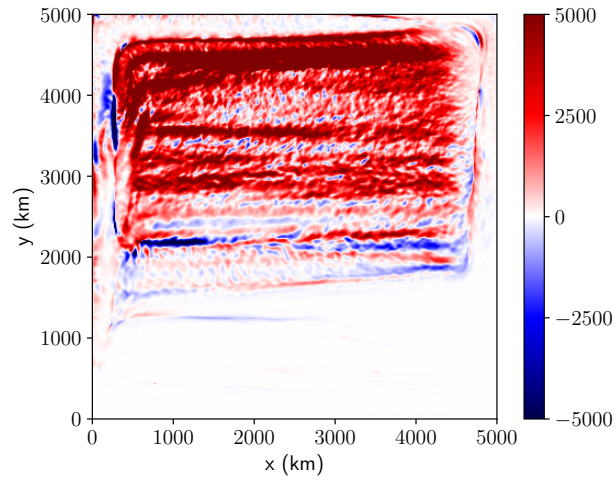


Figure 7: Eddy diffusivity coefficient  $\kappa$  diagnosed as  $\overline{\nabla Q} \cdot \overline{uq} / |\overline{\nabla Q}|^2$  in the upper level (units are  $m^2 s^{-1}$ ).

501 The horizontal and vertical structure of  $\kappa$  is not uniform (see also Abernathey et al. (2013)).  
 502 Overall the magnitude of  $\kappa$  decreases with depth. In the second and third levels, there are large  
 503 areas where  $\kappa$  is weakly negative (not shown).

504 **4.2 Impact of the eddies on the mean buoyancy field**

505 Ultimately, we want to parameterize the effect of eddies on the mean buoyancy (term  $\mathcal{R}$  in  
 506 Eq. (1b)). As mentioned earlier, there are three strategies to build this parameterization: (i) we  
 507 can compute the eddy induced transport in the QG model and use the eddy induced velocity field  
 508 in the primitive equation coarse resolution model to advect the temperature and salinity fields (and  
 509 also other tracers), (ii) we can compute  $\nabla \cdot \overline{\mathbf{u}b}$  as an estimate of  $\mathcal{R}$ , or (iii) we can compute the  
 510 mean buoyancy forcing  $\overline{\mathcal{F}_b}$  as an estimate of  $\mathcal{R}$  (see Eq. 25).

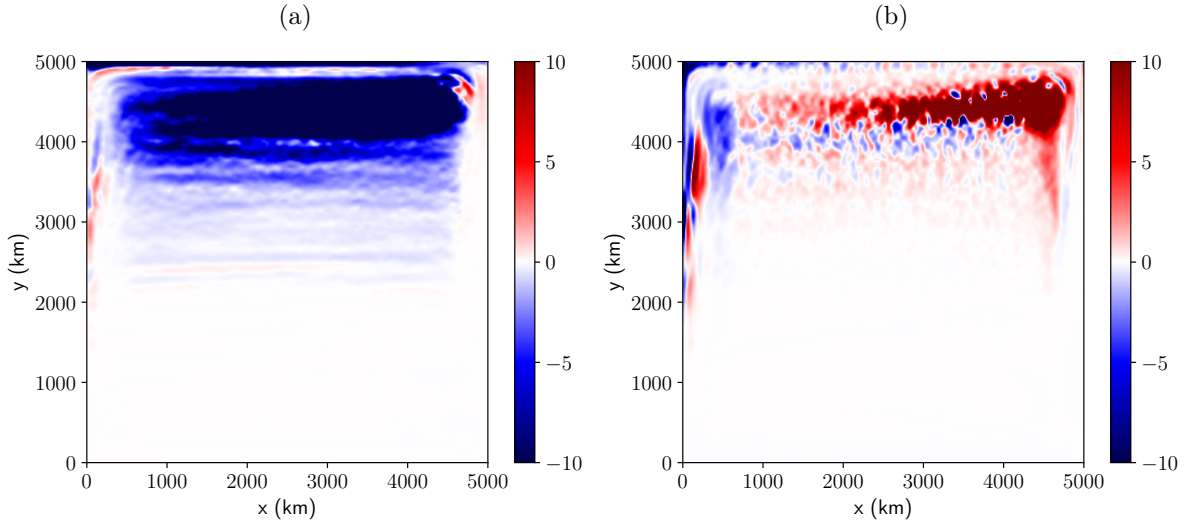


Figure 8: (a): zonal component and (b) meridional component of the upper layer eddy induced transport  $\Upsilon$  in the QG model, as defined in Eq. (21). Units:  $\text{m}^2 \text{s}^{-1}$ . (Same as Fig. 3 but in the QG model)

511 For the first strategy, we need to compute the eddy induced transport. In the QG framework,  
 512 this transport is defined in Eq. (21). We plot both components of the eddy induced transport  $\Upsilon$   
 513 in Fig. 8. These plots compare well with the reference case (Fig. 3): the location and the mag-  
 514 nitude of the maxima matches what we had in the full model.

515 For the second and third strategies, we plot  $-\nabla \cdot \overline{\mathbf{u}b}$  and  $\overline{\mathcal{F}_b}$  in Fig. 9. These two terms cor-  
 516 respond to the buoyancy forcing term  $\mathcal{R}$  and they are not equal simply because we did not run  
 517 the model for a sufficiently long time, and because the divergence of the eddy buoyancy flux is  
 518 slower to converge than  $\mathcal{F}_b$  (see Fig. 10). The plots in Fig. 9 illustrate the warming and cooling  
 519 tendency (if we interpret buoyancy as temperature) due to the eddies on the large-scale solution.  
 520 We observe alternating cooling and warming patterns in the western boundary and in the gyre

521 which are unfortunately relatively hard to interpret as is. In order to get more physical insight into  
 522 how this terms acts on the mean flow, we can convert the buoyancy forcing to a temperature forc-  
 523 ing: as an indication, the dark blue patch in the western boundary corresponds to a forcing of 4 K/year  
 524 and the light red patch in the northern part of the gyre corresponds to a temperature forcing of  
 525 0.4 K/year.

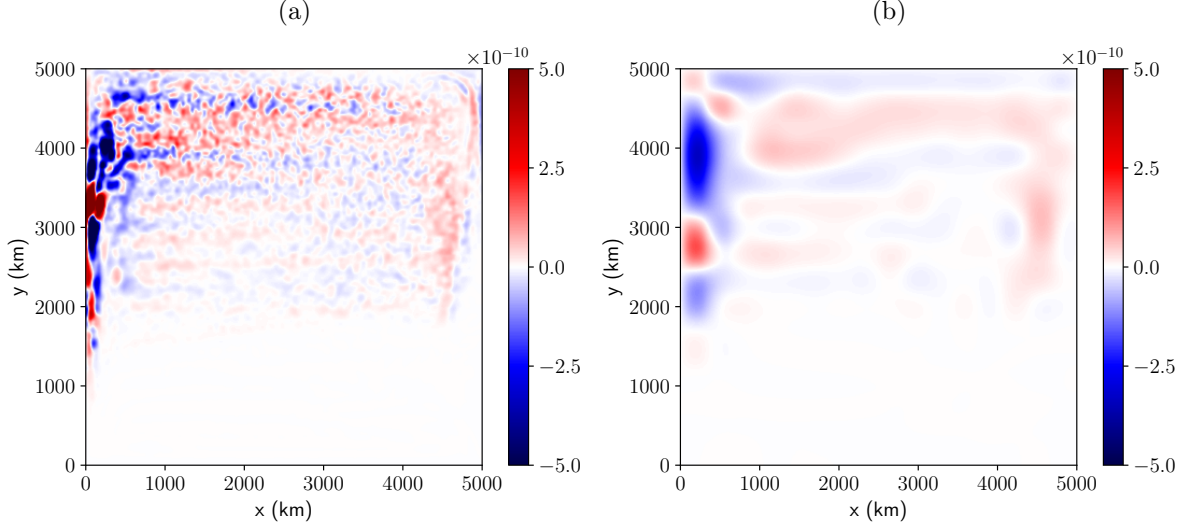


Figure 9: (a)  $-\nabla \cdot \overline{ub}$  smoothed in the upper buoyancy level. (b) Color:  $\overline{F_b}$  in the same level.  
 (units in both plots:  $\text{m s}^{-3}$ )

### 526 4.3 Intermittency of the rectification

527 With the MSQG model, we are able to diagnose the average rectification term as an alter-  
 528 native to the standard GM parameterizations. But there is actually more information available  
 529 in the QG dynamics than just the average feedback  $\nabla \cdot \overline{ub}$  because the term  $\nabla \cdot (ub)$  is a func-  
 530 tion of time. So far, we have only focused on the time mean rectification. In order to build a rec-  
 531 tification term that takes into account this variability, one could use a long time series of  $\nabla \cdot (ub)$   
 532 to extract the variability patterns and add one or several modes of this variability to the mean in  
 533 the rectification term (Li et al., 2023). As a starting point, we document here the first moments  
 534 of the distribution of the eddy statistics, in a similar way as what was proposed by Grooms (2016)  
 535 and Grooms & Kleiber (2019)

536 We first note the auto-correlation of  $\nabla \cdot (ub)$  between two consecutive outputs (30 days)  
 537 is below 0.2 in most of the domain (not shown). Hence, two consecutive output of  $\nabla \cdot (ub)$  can

538 be considered close to independent from each other. This result is consistent with Porta Mana  
 539 & Zanna (2014) who found that the decorrelation time of the eddy rectification term is on the or-  
 540 der of days (see also Samelson et al., 2019, for a similar analysis with SSH fields). As for any ran-  
 541 dom time series, the time scale needed to build a significant mean depends on the statistical mo-  
 542 ments of the distribution.

543 We first plot in Fig. 10 the standard deviation of  $\nabla \cdot (\mathbf{ub})$  and  $\mathcal{F}_b$ . This figure highlights  
 544 the chaotic regions of the dynamics. These regions are directly related to the high eddy activity  
 545 in some parts of the domain (see Fig. 4). Predicting the location of these zone with a linear in-  
 546 stability analysis only (i.e. without the non-linear QG model) seems hard to do: the zones of high  
 547 eddy variability do not directly correspond to zones of maximum instability growth rate (not shown).  
 548 In fact regions of high variability extend well beyond the zone with high linear growth rate. This  
 549 is because once formed, eddies are advected away from their formation site and may drive an in-  
 550 verse cascade in sites that are weakly unstable. The discrepancies between the location of the most  
 551 unstable modes and the location of maximum eddy activity illustrates the fact that the large-scale  
 552 rectification by the small scale eddies is not necessarily a local process and our strategy of ex-  
 553 plicitly modeling the small scale variability can capture this effect. These structures also reflect  
 554 the fact that the inverse cascade is not uniform either in space or in time.

555 The standard deviation of the sample mean is given by  $\sigma/\sqrt{n}$  with  $n$  the sample size. We  
 556 can use this definition to get the error bar on the mean fields that we showed in the previous sec-  
 557 tion. If we focus on  $\mathcal{F}_b$ , we see in Fig. 9 that the order of magnitude of the mean is  $\sim 10^{-10} \text{ m s}^{-3}$   
 558 and in Fig. 10 we see that the order of magnitude of the standard deviation of that same field is  
 559 also  $\sim 10^{-10} \text{ m s}^{-3}$ . Since our sample size is 400 points (33 year time series with 30 day output),  
 560 we estimate that we have 5% error on the field  $\overline{\mathcal{F}_b}$ . Because the standard deviation of  $\nabla \cdot (\mathbf{ub})$   
 561 is 20 times bigger than the standard deviation of  $\mathcal{F}_b$  and if we consider that the mean should be  
 562 identical, then the error on the field  $\nabla \cdot \overline{\mathbf{ub}}$  is on the order of 25%. If we wanted a 5% error on  
 563 this field, we would need a 1000 year time series. This time scale is bigger than the thermocline  
 564 time scale. This implies that eddies could in principle drive low-frequency variability at the ther-  
 565 mocline scale and this variability would itself be modulated by the slow evolution of the thermo-  
 566 cline (Berloff et al., 2007)

567 There are two ways we can use this information to incorporate elements of the eddy vari-  
 568 ability in the GM parameterization. Depending on how we want to represent eddies in the coarse  
 569 resolution model, we can construct a rectification term  $\mathcal{R}$  that is anywhere between a snapshot

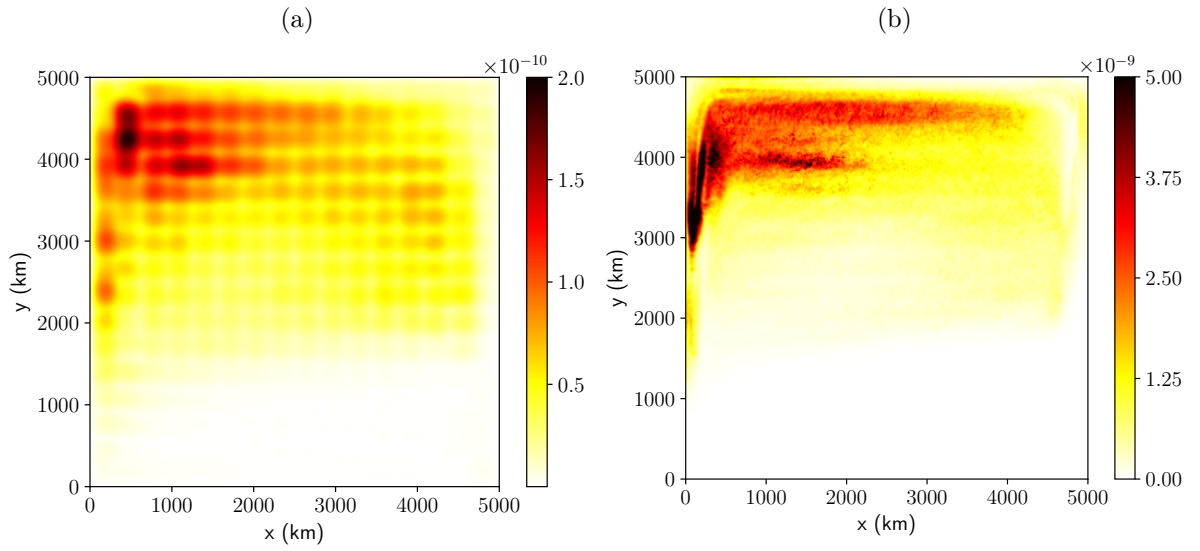


Figure 10: (a): Standard deviation of  $\mathcal{F}_b$  and (b): standard deviation of  $\nabla \cdot (\mathbf{u}b)$  (units  $\text{m s}^{-3}$ )

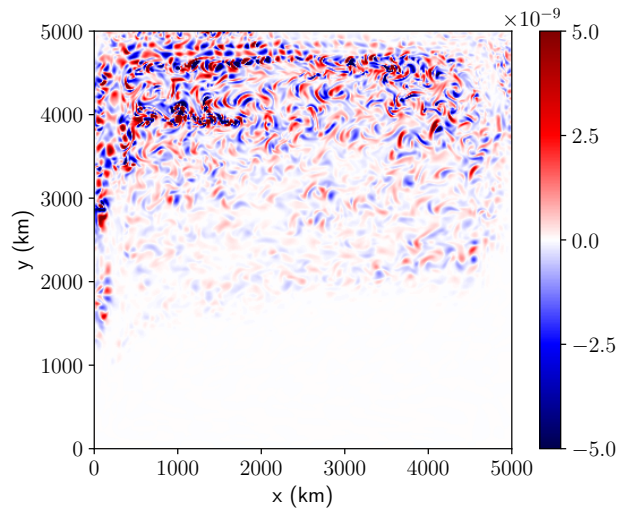


Figure 11: Snapshot of  $\nabla \cdot (\mathbf{u}b)$  in the upper buoyancy level of the QG model.

570  $\mathcal{F}_b$  and the absolute mean  $\overline{\mathcal{F}_b}$  depending on the degree of variability that one wish to add to  $\mathcal{R}$   
 571 and compute the corresponding time varying eddy induced velocity.

572 If we do not want to implement a QG model, another possibility to get a time variable GM  
 573 is simply to add noise in the eddy induced transport  $\Upsilon$ . With this formulation, we depart from  
 574 Grooms & Kleiber (2019) because we propose to model the stochastic component of the param-  
 575 eterization as an additive noise. To illustrate the type of noise, we plot in Fig. 11 a snapshot of  
 576  $\nabla \cdot (ub)$ . We computed a power spectra of this field a got a curve that is relatively flat in the 50km-  
 577 500km range and falls off outside of that range (not shown). One possibility to add a stochastic  
 578 component to GM would be to add to the GM mean a white noise field in this wavelength band.  
 579 We can further characterize the type of noise with the skewness (S) and excess kurtosis (K) of  
 580  $\mathcal{F}_b$ . In most of the domain,  $|S| < 2$  and  $|K| < 2$  such that both the skewness and kurtosis are not  
 581 significantly different from zero. Hence the variability of the rectification could be modeled as  
 582 a random process normally distributed, we suggest that we can formulate the rectification as a  
 583 Wiener process where the amplitude of the noise needs to be learned with a series of realizations  
 584 of the QG model.

## 585 **5 Conclusion**

586 We implemented a prototype multiple-scale quasi-geostrophic model for which the large-  
 587 scale component is described by the average flow of a full eddy resolving model and the small-  
 588 scale component is described by QG dynamics (Pedlosky, 1984; Grooms et al., 2011). In this con-  
 589 text, QG dynamics is solely forced by the baroclinic instability of the large-scale flow. The main  
 590 originality of this implementation is to deploy the QG model at the basin scale such that the strat-  
 591 ification (or equivalently the deformation radii) and the large-scale flow are slowly varying in space.  
 592 This contrasts with the traditional QG implementation where these large-scale variables (strat-  
 593 ification and background flow) are uniform over the QG domain. This new model is well suited  
 594 to study the full instability problem in ocean gyres: the main advantage of this new implemen-  
 595 tation is to relax the locality hypothesis which assumes that oceanic eddies are generated locally  
 596 and interact only locally with the large-scale flow (Venaille et al., 2011; Tulloch et al., 2011). A  
 597 comparison between the MSQG model and the reference primitive equation model shows good  
 598 agreement between the two eddy dynamics. We then focused on the different methods to use the  
 599 QG model to rectify the background flow. In this article, we showed that, the inverse cascade re-  
 600 mains weak (on the same order as bottom friction). However, the nature of the solution would  
 601 be different without the large-scale filtering (the same remark applies for bottom friction). The

602 consequence of this inverse cascade is that the small-scale flow rectifies the large-scale flow. This  
603 claim was also what was anticipated by Gent & McWilliams (1990) when they proposed a pa-  
604 rameterization of ocean eddies. In our paper, we have compared GM fluxes with the fluxes com-  
605 puted with a model of intermediate complexity that explicitly resolves eddy dynamics. We find  
606 good agreement between the QG model and the reference primitive equation model such that ed-  
607 dies flatten isopycnal surfaces (or homogenize PV) with a diffusivity coefficient on the order of  
608  $10^3 - 10^4 \text{ m}^2 \text{ s}^{-1}$ . We also showed that in specific places eddies can strengthen the large-scale  
609 flow by fluxing PV up the mean gradient. The fact that we could not get a converged field of  $\nabla \cdot$   
610  $\overline{ub}$  after 30 years of integration even after applying a spatial smoothing, raises an interesting con-  
611 cern: it is probably pointless to parameterize the eddy as a stationary response. The eddy response  
612 inevitably contains a time-variable part that we can capture with the QG model.

613 This multiple scale model offers many possibilities for process oriented studies. The im-  
614 mediate extension of this work is to study the full super-parameterization implementation where  
615 the mean flow comes from a coarse resolution model and the eddy feedback is effectively added  
616 to the mean flow. We anticipate that the rectification of the large-scale flow by small scale ed-  
617 dies will have two effects: first it will change the background flow seen by the QG model. This  
618 change will modify the strength of the baroclinic instabilities (Farrell & Ioannou, 1999; Flierl &  
619 Pedlosky, 2007). But most importantly, it will drive an additional air-sea flux in an attempt to re-  
620 store the initial large-scale solution. Because we observed strong variability in the rectification  
621 process, we conjecture that a coupled model will exhibit low-frequency modes of variability via  
622 this mechanism. The coupled model is also well suited to revisit the dynamics of the ventilated  
623 thermocline in the presence of eddies and see how the conservation of large-scale potential vor-  
624 ticity is modulated by the PV homogenization due to small-scale eddies (Dereble & Dewar, 2013).  
625 Eddy-mean flow is also a key interaction in the Antarctic circumpolar current (ACC) because a  
626 large fraction of the mass and heat transport is carried out by eddies (Cessi et al., 2006). Many  
627 conceptual models of the ACC rely on a parameterization of oceanic eddies to establish the ver-  
628 tical structure of the isopycnal layers (Marshall & Radko, 2003; Nikurashin & Vallis, 2012). This  
629 multiple scale model offers an alternative to these parameterized models and could help validate  
630 or adjust theoretical models on the residual circulation in the ACC.

631 Another aspect that we have only briefly mentioned is the effect of the seasonal cycle. The  
632 seasonal time scale is between the eddy time scale and the planetary time scale and should have  
633 a strong impact on both systems. In particular, the seasonal cycle will have an impact on the deep  
634 convection areas, and will also affect the depth of the mixed layer. These changes may locally

635 enhance the eddy dynamics and thus affect the coupled system. There are possibilities to explore  
 636 this variability (Uchida et al., 2021). The extension to the MSQG model is clearly possible but  
 637 is beyond the scope of this study.

## 638 **Open Research Section**

639 The configuration file for the MITgcm runs are here [https://github.com/bderembl/  
 640 mitgcm\\_configs/tree/master/natl\\_square](https://github.com/bderembl/mitgcm_configs/tree/master/natl_square). The source code for the multiple scale QG  
 641 model is here <https://github.com/bderembl/msom> (Deremble & Martinez, 2020).

## 642 **Acknowledgments**

643 This work is supported by NSF grants 1434780, 1537304. TU and WKD acknowledge the sup-  
 644 port from the NSF grant OCE-2023585, OCE-2123632, and the French ‘Make Our Planet Great  
 645 Again’ (MOPGA) program managed by the Agence Nationale de la Recherche under the Programme  
 646 d’Investissement d’Avenir, reference ANR-18-MPGA-0002. Research support for RMS was pro-  
 647 vided by NASA (National Aeronautics and Space Administration) grants NNX13AD78G, NNX16AH76G  
 648 and 80NSSC21K1188. We thank D. Balwada, P. Cessi, I. Grooms, B. Gallet and K. Julien for  
 649 their insightful comments and discussions.

## 650 **References**

- 651 Abernathey, R., Ferreira, D., & Klocker, A. (2013, December). Diagnostics of isopycnal  
 652 mixing in a circumpolar channel. *Ocean Model.*, *72*, 1-16. doi: 10.1016/j.ocemod.2013.07  
 653 .004
- 654 Bachman, S. D. (2019). The gm+ e closure: A framework for coupling backscatter with  
 655 the gent and mcwilliams parameterization. *Ocean Model.*, *136*, 85–106. doi: 10.1016/j.  
 656 .ocemod.2019.02.006
- 657 Berloff, P., Hogg, A. M., & Dewar, W. (2007). The turbulent oscillator: A mechanism of  
 658 low-frequency variability of the wind-driven ocean gyres. *J. Phys. Oceanogr.*, *37*, 2363–  
 659 2386. doi: 10.1175/JPO3118.1
- 660 Cessi, P. (2008). An energy-constrained parameterization of eddy buoyancy flux. *J. Phys.*  
 661 *Oceanogr.*, *38*(8), 1807–1819.
- 662 Cessi, P., Young, W. R., & Polton, J. A. (2006). Control of large-scale heat transport by  
 663 small-scale mixing. *J. Phys. Oceanogr.*, *36*, 1877. doi: 10.1175/JPO2947.1
- 664 Colin de Verdiere, A. (1986). On mean flow instabilities within the planetary geostrophic

- 665 equations. *J. Phys. Oceanogr.*, *16*, 1981–1984. doi: 10.1175/1520-0485(1986)016<1981:  
 666 OMFIWT>2.0.CO;2
- 667 Cushman-Roisin, B., & Beckers, J.-M. (2011). *Introduction to geophysical fluid dynamics:  
 668 physical and numerical aspects* (Vol. 101). Academic Press.
- 669 Deremble, B., & Dewar, W. K. (2013). Volume and potential vorticity budgets of Eighteen  
 670 Degree Water. *J. Phys. Oceanogr.*, *43*, 2309–2321. doi: 10.1175/JPO-D-13-052.1
- 671 Deremble, B., Johnson, E. R., & Dewar, W. K. (2017). A coupled model of interior balanced  
 672 and boundary flow. *Ocean Model.*, *119*, 1–12. doi: 10.1016/j.ocemod.2017.09.003
- 673 Deremble, B., & Martinez, E. M. (2020). MSOM: *Multiple scale ocean model*. Retrieved from  
 674 <https://github.com/bderembl/msom> doi: 10.5281/zenodo.4669909
- 675 Dewar, W. K., Samelson, R. M., & Vallis, G. K. (2005). The ventilated pool: A model of  
 676 subtropical mode water. *J. Phys. Oceanogr.*, *35*, 137–150. doi: 10.1175/JPO-2681.1
- 677 Eden, C., & Greatbatch, R. J. (2008). Towards a mesoscale eddy closure. *Ocean Model.*,  
 678 *20*(3), 223–239.
- 679 Farrell, B. F., & Ioannou, P. J. (1999). Perturbation growth and structure in time-dependent  
 680 flows. *J. Atmos. Sci.*, *56*, 3622–3639. doi: 10.1175/1520-0469(1999)056<3622:PGASIT>  
 681 2.0.CO;2
- 682 Ferrari, R., Griffies, S. M., Nurser, A. J. G., & Vallis, G. K. (2010). A boundary-value prob-  
 683 lem for the parameterized mesoscale eddy transport. *Ocean Model.*, *32*, 143–156. doi: 10  
 684 .1016/j.ocemod.2010.01.004
- 685 Ferrari, R., McWilliams, J. C., Canuto, V. M., & Dubovikov, M. (2008). Parameterization of  
 686 eddy fluxes near oceanic boundaries. *J. Climate*, *21*(12), 2770–2789.
- 687 Flierl, G. R., & Pedlosky, J. (2007). The nonlinear dynamics of time-dependent subcritical  
 688 baroclinic currents. *J. Phys. Oceanogr.*, *37*, 1001–1021. doi: 10.1175/JPO3034.1
- 689 Gent, P. R. (2011). The gent–mcwilliams parameterization: 20/20 hindsight. *Ocean Model.*,  
 690 *39*(1-2), 2–9.
- 691 Gent, P. R., & McWilliams, J. C. (1990). Isopycnal mixing in ocean circulation models.  
 692 *J. Phys. Oceanogr.*, *20*, 150–160. doi: 10.1175/1520-0485(1990)020<0150:IMIOCM>2.0  
 693 .CO;2
- 694 Gnanadesikan, A., Pradal, M.-A., & Abernathey, R. (2015). Isopycnal mixing by mesoscale  
 695 eddies significantly impacts oceanic anthropogenic carbon uptake. *Geophys. Res. Lett.*,  
 696 *42*(11), 4249–4255.
- 697 Griffies, S. M. (1998). The Gent McWilliams skew flux. *J. Phys. Oceanogr.*, *28*, 831–841.

- 698 doi: 10.1175/1520-0485(1998)028<0831:TGMSF>2.0.CO;2
- 699 Griffies, S. M., Winton, M., Anderson, W. G., Benson, R., Delworth, T. L., Dufour, C. O.,  
700 . . . others (2015). Impacts on ocean heat from transient mesoscale eddies in a hierarchy  
701 of climate models. *J. Climate*, 28(3), 952–977. doi: 10.1175/JCLI-D-14-00353.1
- 702 Grooms, I. (2016, October). A gaussian-product stochastic gent-mcwilliams parameteriza-  
703 tion. *Ocean Model.*, 106, 27–43. doi: 10.1016/j.ocemod.2016.09.005
- 704 Grooms, I., Julien, K., & Fox-Kemper, B. (2011). On the interactions between plan-  
705 etary geostrophy and mesoscale eddies. *Dyn. Atmos. Ocean*, 51, 109–136. doi:  
706 10.1016/j.dynatmoce.2011.02.002
- 707 Grooms, I., & Kleiber, W. (2019, January). Diagnosing, modeling, and testing a multiplica-  
708 tive stochastic gent-mcwilliams parameterization. *Ocean Model.*, 133, 1–10. doi: 10.1016/  
709 j.ocemod.2018.10.009
- 710 Guillaumin, A. P., & Zanna, L. (2021). Stochastic-deep learning parameterization of ocean  
711 momentum forcing. *J. Adv. Model. Earth Syst.*, 13(9), e2021MS002534. doi: 10.1029/  
712 2021MS002534
- 713 Hogg, A. M., Dewar, W. K., Killworth, P. D., & Blundell, J. R. (2003). A quasi-geostrophic  
714 coupled model (Q-GCM). *Mon. Wea. Rev.*, 131(10), 2261–2278. doi: 10.1175/1520  
715 -0493(2003)131<2261:AQCMQ>2.0.CO;2
- 716 Jackson, L., Hughes, C. W., & Williams, R. G. (2006, January). Topographic control of basin  
717 and channel flows: The role of bottom pressure torques and friction. *J. Phys. Oceanogr.*,  
718 36(9), 1786–1805. doi: 10.1175/JPO2936.1
- 719 Jamet, Q., Deremble, B., Wienders, N., Uchida, T., & Dewar, W. (2021). On wind-driven en-  
720 ergetics of subtropical gyres. *J. Adv. Model. Earth Syst.*, 13(4), e2020MS002329. doi: 10  
721 .1029/2020MS002329
- 722 Jansen, M. F., Adcroft, A., Khani, S., & Kong, H. (2019). Toward an energetically consistent,  
723 resolution aware parameterization of ocean mesoscale eddies. *J. Adv. Model. Earth Syst.*,  
724 11(8), 2844–2860. doi: 10.1029/2019MS001750
- 725 Juricke, S., Danilov, S., Kutsenko, A., & Oliver, M. (2019). Ocean kinetic energy backscatter  
726 parametrizations on unstructured grids: Impact on mesoscale turbulence in a channel.  
727 *Ocean Model.*, 138, 51–67. doi: 10.1016/j.ocemod.2019.03.009
- 728 Killworth, P. D., & Blundell, J. R. (2007). Planetary wave response to surface forcing and in-  
729 stability in the presence of mean flow and topography. *J. Phys. Oceanogr.*, 37, 1297–1320.  
730 doi: 10.1175/JPO3055.1

- 731 Li, L., Deremble, B., Lahaye, N., & Mémin, E. (2023). Stochastic data-driven parameter-  
732 ization of unresolved eddy effects in a baroclinic quasi-geostrophic model. *J. Adv. Model.*  
733 *Earth Syst.*, 15(2), e2022MS003297. doi: 10.1029/2022MS003297
- 734 Mak, J., Avdis, A., David, T., Lee, H. S., Na, Y., Wang, Y., & Yan, F. E. (2022). On con-  
735 straining the mesoscale eddy energy dissipation time-scale. *J. Adv. Model. Earth Syst.*,  
736 14(11), e2022MS003223.
- 737 Mak, J., Marshall, D. P., Maddison, J. R., & Bachman, S. D. (2017). Emergent eddy satura-  
738 tion from an energy constrained eddy parameterisation. *Ocean Model.*, 112, 125–138.
- 739 Marshall, D. P., Maddison, J. R., & Berloff, P. S. (2012). A framework for parameterizing  
740 eddy potential vorticity fluxes. *J. Phys. Oceanogr.*, 42(4), 539–557. doi: 10.1175/JPO-D-  
741 -11-048.1
- 742 Marshall, J., Adcroft, A., Hill, C., Perelman, L., & Heisey, C. (1997). A finite-volume, in-  
743 compressible Navier Stokes model for studies of the ocean on parallel computers. *J. Geo-*  
744 *phys. Res.*, 102, 5753–5766. doi: 10.1029/96JC02775
- 745 Marshall, J., & Radko, T. (2003). Residual-mean solutions for the antarctic circumpolar cur-  
746 rent and its associated overturning circulation. *J. Phys. Oceanogr.*, 33, 2341–2354. doi: 10  
747 .1175/1520-0485(2003)033<2341:RSFTAC>2.0.CO;2
- 748 McDougall, T. J., & McIntosh, P. C. (2001). The temporal-residual-mean velocity. part  
749 II: Isopycnal interpretation and the tracer and momentum equations. *J. Phys. Oceanogr.*,  
750 31(5), 1222–1246.
- 751 Mémin, E. (2014, March). Fluid flow dynamics under location uncertainty. *Geophys. Astro.*  
752 *Fluid.*, 108, 119–146. doi: 10.1080/03091929.2013.836190
- 753 Meunier, J., Miquel, B., & Gallet, B. (2023). A direct derivation of the gent-mcwilliams/redi  
754 diffusion tensor from quasi-geostrophic dynamics. *J. Fluid Mech.*, 963, A22.
- 755 Nakamura, M., & Chao, Y. (2000, January). On the eddy isopycnal thickness diffusivity of  
756 the gent-mcwilliams subgrid mixing parameterization. *J. Climate*, 13(2), 502–510. doi: 10  
757 .1175/1520-0442(2000)013<0502:OTEITD>2.0.CO;2
- 758 Nikurashin, M., & Vallis, G. K. (2012). A theory of the interhemispheric meridional over-  
759 turning circulation and associated stratification. *J. Phys. Oceanogr.*, 42, 1652-1667. doi:  
760 10.1175/JPO-D-11-0189.1
- 761 Pedlosky, J. (1984). The equations for geostrophic motion in the ocean. *J. Phys. Oceanogr.*,  
762 14, 448–456. doi: 10.1175/1520-0485(1984)014<0448:TEFGMI>2.0.CO;2
- 763 Pedlosky, J. (1987). *Geophysical fluid dynamics, 2nd ed.* New York and Berlin: Springer-

- 764 Verlag, 1982. (636 pp.)
- 765 Porta Mana, P., & Zanna, L. (2014). Toward a stochastic parameterization of ocean  
766 mesoscale eddies. *Ocean Model.*, 79, 1–20. doi: 10.1016/j.ocemod.2014.04.002
- 767 Rhines, P. B., & Young, W. R. (1982). Homogenization of potential vorticity in planetary  
768 gyres. *J. Fluid Mech.*, 122, 347–367. doi: 10.1017/S0022112082002250
- 769 Rouillet, G., McWilliams, J. C., Capet, X., & Molemaker, M. J. (2012). Properties of steady  
770 geostrophic turbulence with isopycnal outcropping. *J. Phys. Oceanogr.*, 42, 18–38. doi: 10  
771 .1175/JPO-D-11-09.1
- 772 Ryzhov, E. A., Kondrashov, D., Agarwal, N., McWilliams, J. C., & Berloff, P. (2020). On  
773 data-driven induction of the low-frequency variability in a coarse-resolution ocean model.  
774 *Ocean Model.*, 153, 101664. doi: 10.1016/j.ocemod.2020.101664
- 775 Salmon, R. (1994). Generalized two-layer models of ocean circulation. *J. Mar. Res.*, 52(5),  
776 865–908. doi: doi:10.1357/0022240943076939
- 777 Samelson, R., & Vallis, G. K. (1997). Large-scale circulation with small diapycnal diffusion:  
778 The two-thermocline limit. *J. Mar. Res.*, 55(2), 223–275.
- 779 Samelson, R. M., Chelton, D. B., & Schlax, M. G. (2019). The ocean mesoscale regime of  
780 the reduced-gravity quasigeostrophic model. *J. Phys. Oceanogr.*, 49(10), 2469–2498. doi:  
781 10.1175/JPO-D-18-0260.1
- 782 Samelson, R. M., & Vallis, G. K. (1997). A simple friction and diffusion scheme for plan-  
783 etary geostrophic basin models. *J. Phys. Oceanogr.*, 27, 186–194. doi: 10.1175/1520  
784 -0485(1997)027<0186:ASFADS>2.0.CO;2
- 785 Shevchenko, I. V., & Berloff, P. S. (2015). Multi-layer quasi-geostrophic ocean dynamics in  
786 eddy-resolving regimes. *Ocean Model.*, 94, 1–14. doi: 10.1016/j.ocemod.2015.07.018
- 787 Simonnet, E., Rolland, J., & Bouchet, F. (2021, June). Multistability and rare spontaneous  
788 transitions in barotropic beta-plane turbulence. *J. Atmos. Sci.*, 78(6), 1889-1911. doi: 10  
789 .1175/JAS-D-20-0279.1
- 790 Smith, K. (2007). The geography of linear baroclinic instability in earth’s oceans. *J. Mar.*  
791 *Res.*, 65(5), 655–683. doi: 10.1357/002224007783649484
- 792 Stewart, A. L., McWilliams, J. C., & Solodoch, A. (2021, May). On the role of bottom pres-  
793 sure torques in wind-driven gyres. *J. Phys. Oceanogr.*, 51(5), 1441-1464. doi: 10.1175/  
794 JPO-D-20-0147.1
- 795 Theiss, J. (2006). A generalized rhines effect and storms on jupiter. *Geophys. Res. Lett.*, 33,  
796 L08809. doi: 10.1029/2005GL025379

- 797 Toggweiler, J. R., & Samuels, B. (1995). Effect of drake passage on the global thermohaline  
798 circulation. *Deep-Sea Res. (I Oceanogr. Res. Pap.)*, *42*(4), 477–500. doi: 10.1016/0967  
799 -0637(95)00012-U
- 800 Treguier, A. M., Held, I. M., & Larichev, V. D. (1997). Parameterization of quasigeostrophic  
801 eddies in primitive equation ocean models. *J. Phys. Oceanogr.*, *27*, 567–580. doi: 10  
802 .1175/1520-0485(1997)027<0567:POQEIP>2.0.CO;2
- 803 Tulloch, R., Marshall, J., Hill, C., & Smith, K. S. (2011). Scales, growth rates, and spectral  
804 fluxes of baroclinic instability in the ocean. *J. Phys. Oceanogr.*, *41*, 1057–1076. doi: 10  
805 .1175/2011JPO4404.1
- 806 Uchida, T. (2019). *Seasonality in surface (sub) mesoscale turbulence and its impact on iron*  
807 *transport and primary production* (Doctoral dissertation, Columbia University in the City  
808 of New York). doi: 10.7916/d8-9s8r-m049
- 809 Uchida, T., Deremble, B., & Penduff, T. (2021). The seasonal variability of the ocean energy  
810 cycle from a quasi-geostrophic double gyre ensemble. *Fluids*, *6*(6), 206. doi: 10.3390/  
811 fluids6060206
- 812 Uchida, T., Deremble, B., & Popinet, S. (2022). Deterministic model of the eddy dynamics  
813 for a midlatitude ocean model. *J. Phys. Oceanogr.*, *52*(6), 1133–1154. doi: 10.1175/JPO  
814 -D-21-0217.1
- 815 Vallis, G. K. (2017). *Atmospheric and oceanic fluid dynamics: Fundamentals and large-*  
816 *scale circulation* (2nd ed.). Cambridge University Press.
- 817 Venaille, A., Vallis, G. K., & Smith, K. S. (2011, September). Baroclinic turbulence in  
818 the ocean: Analysis with primitive equation and quasigeostrophic simulations. *J. Phys.*  
819 *Oceanogr.*, *41*, 1605–1623. doi: 10.1175/JPO-D-10-05021.1
- 820 Visbeck, M., Marshall, J., Haine, T., & Spall, M. (1997). Specification of eddy transfer co-  
821 efficients in coarse-resolution ocean circulation models. *J. Phys. Oceanogr.*, *27*(3), 381–  
822 402.
- 823 Warren, B. A. (1990). Suppression of deep oxygen concentrations by drake passage. *Deep-*  
824 *Sea Res. (I Oceanogr. Res. Pap.)*, *37*(12), 1899–1907. doi: 10.1016/0198-0149(90)90085  
825 -A
- 826 Waterman, S., & Jayne, S. R. (2011, April). Eddy-mean flow interactions in the along-  
827 stream development of a western boundary current jet: An idealized model study. *J. Phys.*  
828 *Oceanogr.*, *41*(4), 682–707. doi: 10.1175/2010JPO4477.1
- 829 Wunsch, C., & Ferrari, R. (2004). Vertical mixing, energy, and the general circulation of

the oceans. *Annu. Rev. Fluid Mech.*, *36*, 281–314. doi: 10.1146/annurev.fluid.36.050802  
 .122121

Zhao, R., & Vallis, G. (2008). Parameterizing mesoscale eddies with residual and eulerian  
 schemes, and a comparison with eddy-permitting models. *Ocean Model.*, *23*, 1–12.

## Appendix A Other QG configurations

### A1 MSQG without $\mathcal{F}_q$

We argued in the main text, that the purpose of the term  $\mathcal{F}_q$  in Eq. (8) is to ensure that  $\overline{\psi'} = \overline{q'} = 0$ . It is however possible to run the MSQG model without this term (i.e.  $\mathcal{F}_q = 0$ ). In this case, the solution converges to a different statistical equilibrium than the one we described in section 3.2. We plot in Fig. A1 the same kinetic energy figures (snapshot of kinetic energy and mean kinetic energy) that we have been plotting to do the model comparison. Although Fig. A1 has a lot of common features with the reference run (Fig. 2), we emphasize that this run now exhibit a mean flow ( $\overline{\psi'} \neq 0$ ). To highlight this mean flow, we plot in Fig. A2 the upper level time mean stream function with the same contour interval as Fig. 1. In this figure, we see indications that the MSQG model tends to create a large-scale flow equal and opposite to the prescribed large-scale flow. This is the case near the northern and southern boundaries. We interpret these two features as an attempt of the MSQG equation to restore a state of rest ( $\psi + \Psi = 0$ ). Slightly off from the western boundary, the model creates a strong northward mean flow at the central latitude which can be seen as an intensification of the western boundary current. And near the eastern boundary, we see a mean southward flow which is here harder to explain. However, since we believe the build up of this large-scale flow in the small-scale equation is spurious we do not want to comment too much this figure.

### A2 Traditional QG

We also briefly illustrate the type of dynamics that develop in a traditional QG model. The equations of evolution of PV are the same as the one written in this article except that the in the traditional QG, we use a uniform background stratification and uniform Coriolis parameter in the definition of PV (Eq. (4)). For these parameters, we take the mean values of  $N^2$  and  $f$  over the whole domain (we still keep  $N^2$  variable is the vertical dimension and we keep the  $\beta$  effect in the definition of the background PV). This really corresponds to the traditional QG equation albeit

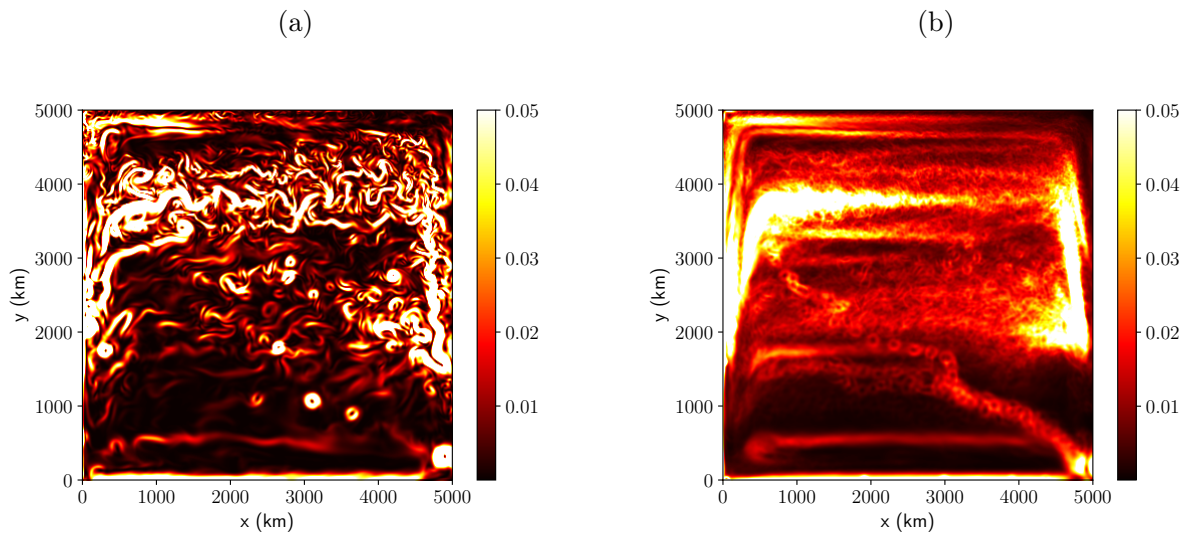


Figure A1: (a) Snapshot of kinetic energy  $E_k$ ; (b) mean kinetic energy. Both fields are in the upper level of the MSQG model without  $\mathcal{F}_q$ . (units are  $\text{m}^2 \text{s}^{-2}$ )

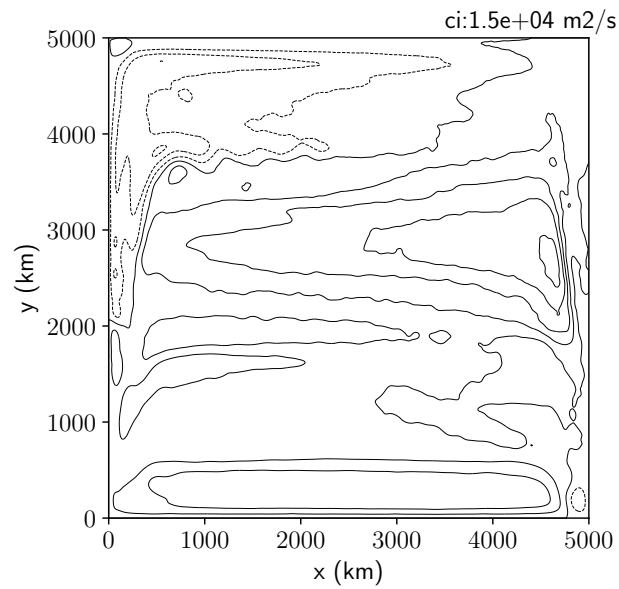


Figure A2: Mean upper level stream function of the MSQG model without  $\mathcal{F}_q$ . Contour intervals are  $1.5 \times 10^4 \text{ m}^2 \text{ s}^{-1}$ , same as Fig. 1a.

859 forced with a non standard background flow. Indeed we keep the same background flow that cor-  
 860 responds the mean velocity field of the reference model.

861 We plot in Fig. A3 a snapshot of KE and the mean KE obtained in this traditional QG model.  
 862 The intensity of the eddy flow is drastically different from the reference model. This is due to the  
 863 fact that for a given value of the background mean flow the stratification cannot be adjusted to  
 864 tame the instability and the flow appears to be much more unstable.

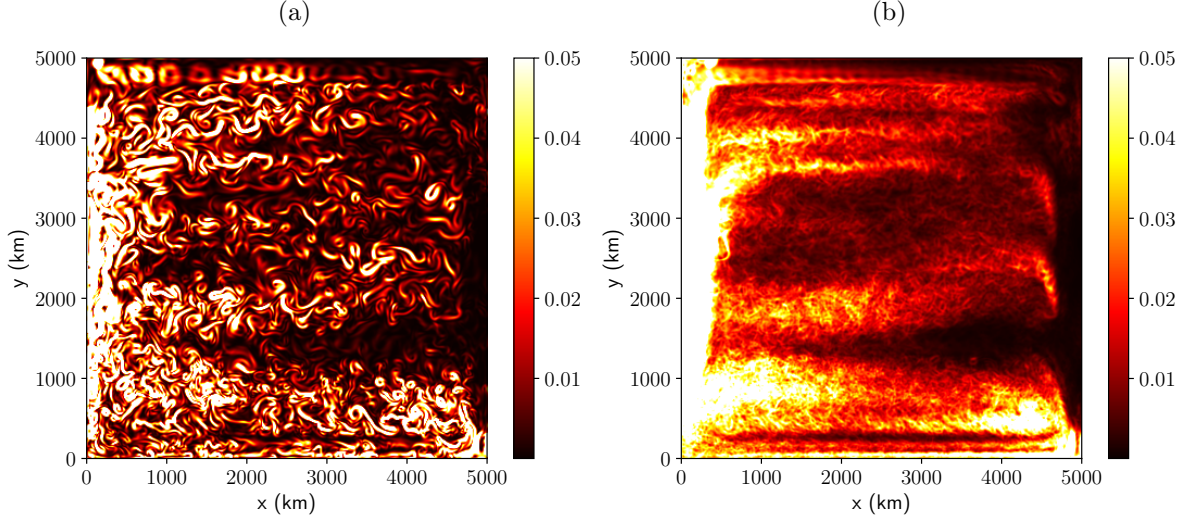


Figure A3: (a) Snapshot of kinetic energy  $E_k$ ; (b) mean kinetic energy in the upper level of the traditional QG model. Units are  $\text{m}^2 \text{s}^{-2}$ . (Same as Fig. 2 but for the traditional QG model.)

## 865 **Appendix B Numerical implementation of the MSQG model**

866 There are several challenges related to the numerical implementation of the multiple scale  
 867 model. We present the highlights of this implementation here.

### 868 **B1 Multiple scale derivatives**

869 In the multiple-scale formalism, small-scale and large-scale variables are defined on two  
 870 different coordinate systems which we denote  $(x, y)$  and  $(X, Y)$  respectively for this appendix only.

871 So taking the large-scale derivative of a small-scale field (and vice versa) is zero

$$\frac{\partial u}{\partial X} = \frac{\partial U}{\partial x} = 0, \quad (\text{B1})$$

872 Moreover, it is important to note that both  $f$  and  $N^2$  are large-scale variables. In the nu-  
 873 merical model, we make sure we do not take spurious spatial derivative of large-scale fields. For  
 874 example, when we compute the gradient of the small-scale PV (for the advective term in Eq. 4),  
 875 we first compute the gradient of the stream function  $\psi$  and then reconstruct the gradient of the  
 876 PV field, as shown here for the  $x$  derivative

$$\frac{\partial q}{\partial x} = \nabla^2 \frac{\partial \psi}{\partial x} + \Gamma \frac{\partial \psi}{\partial x} \quad (\text{B2a})$$

$$\neq \frac{\partial}{\partial x} (\nabla^2 \psi + \Gamma \psi) \quad (\text{B2b})$$

877 If we use Eq. (B2b) instead of Eq. (B2a), the model will exhibit a different dynamics. In  
 878 fact, even the linear stability analysis reveals very different unstable modes depending on the for-  
 879 mulation of the gradient of the large-scale PV (not shown). We recall that the correct definition  
 880 of the gradient of the large-scale PV is given in Eq. (12) (see also Smith, 2007).

## 881 **B2 Definition of the velocity**

882 We do one exception to the rule mentioned above for the definition of the velocity. In the  
 883 original derivation of the multiple scale model, the definition of the small-scale velocity is

$$\mathbf{k} \times \mathbf{u} = -\frac{1}{f} \nabla p, \quad (\text{B3})$$

884 with  $p$  the small-scale pressure. This formulation leads to several issues in the numerical formu-  
 885 lation because (i) the velocity field is divergent, and (ii) with this formulation, the model does not  
 886 conserve kinetic energy (we cannot proceed with the usual integration by part because  $f$  is func-  
 887 tion of space; see below). For these two reasons, we opted for the formulation

$$\mathbf{k} \times \mathbf{u} = -\nabla \psi, \quad (\text{B4})$$

888 which solves the two issues raised above. We verified that the linear instability analysis is very  
 889 similar with both formulations (Eq. (B3) and Eq. (B4)) because the velocity field at each loca-  
 890 tion is almost unchanged with the two formulations. Also, for the same reasons, and in order to  
 891 use the same operators for the small-scale fields and the large-scale fields, we did the same sim-  
 892 plification for definition of the large-scale velocity (see Eq. 10).

893 **B3 Vertical discretization**

894 An important requirement is that the large-scale stratification  $N^2$  must be non zero to avoid  
 895 a singularity in the stretching term of the quasi-geostrophic PV. For that reason, we will imple-  
 896 ment the QG model with a small number of vertical levels (to avoid the vertical discretization of  
 897 the surface mixed layer and the deep ocean). We adjust the values of  $N^2$  to not allow any value  
 898 below  $10^{-6} \text{ s}^{-2}$ .

899 We presented the QG formalism in the continuously stratified framework but once the equa-  
 900 tions are discretized in a numerical model, they are strictly equivalent to the layered equations,  
 901 see (Pedlosky, 1987, chap. 6.18). In fact, we abuse this analogy to include topographic effect and  
 902 bottom drag in the model. They should normally be included as a boundary condition in the bot-  
 903 tom buoyancy field (see Vallis, 2017, section 5.4.3) but we instead add that boundary condition  
 904 in the lower level PV dynamics as is done in the layered formalism (Hogg et al., 2003). In the  
 905 lower level, the gradient of the large-scale vorticity is then

$$\bar{\nabla}Q^l = \left( \Gamma V + \frac{f}{h_l} \frac{\partial h_b}{\partial x}, \beta - \Gamma U + \frac{f}{h_l} \frac{\partial h_b}{\partial y} \right). \quad (\text{B5})$$

906 with  $h_b$  the height of the topography and  $h_l$  the thickness of the lower layer (see Eq. B.2 in Smith,  
 907 2007).

908 **B4 Advection operator**

909 In traditional QG models, the numerical formulation of the advective term is usually done  
 910 with the Arakawa discretization because this formulation ensures the conservation of energy and  
 911 enstrophy (Cushman-Roisin & Beckers, 2011). The Arakawa Jacobian is the sum of three dif-  
 912 ferent discretizations  $J = J^{++} + J^{+\times} + J^{\times+}$ . Let us consider the advection of PV at level  $l$  which  
 913 is defined as

$$q_l = \zeta_l + \Gamma_{l+1}\psi_{l+1} + \Gamma_l\psi_l + \Gamma_{l-1}\psi_{l-1} \quad \text{with} \quad \zeta_l = \nabla^2\psi_l \quad (\text{B6})$$

914 We construct a numerical model of the advection operator (Eq. 8) as

$$\begin{aligned}
 \mathbf{u}_l \cdot \nabla q_l + \mathbf{U}_l \cdot \nabla q_l + \mathbf{u}_l \cdot \overline{\nabla} Q_l &= J(\psi_l, q_l) + J(\Psi_l, q_l) + J(\psi_l, Q_l) \\
 &= J(\psi_l, \zeta_l) + \Gamma_{l+1} J(\psi_l, \psi_{l+1}) + \Gamma_{l-1} J(\psi_l, \psi_{l-1}) \\
 &\quad + J(\Psi_l, \zeta_l) + \Gamma_{l+1} J(\Psi_l, \psi_{l+1}) + \Gamma_{l-1} J(\Psi_l, \psi_{l-1}) + \Gamma_l J(\Psi_l, \psi_l) \\
 &\quad + \Gamma_{l+1} J(\psi_l, \Psi_{l+1}) + \Gamma_{l-1} J(\psi_l, \Psi_{l-1}) + \Gamma_l J(\psi_l, \Psi_l) \\
 &= J(\psi_l, \zeta_l) + J(\Psi_l, \zeta_l) \\
 &\quad + \Gamma_{l+1} J(\psi_l, \psi_{l+1}) - \Gamma_{l-1} J(\psi_{l-1}, \psi_l) \\
 &\quad + \Gamma_{l+1} J(\Psi_l, \psi_{l+1}) - \Gamma_{l-1} J(\Psi_{l-1}, \psi_l) \\
 &\quad + \Gamma_{l+1} J(\psi_l, \Psi_{l+1}) - \Gamma_{l-1} J(\psi_{l-1}, \Psi_l)
 \end{aligned} \tag{B7}$$

915 Note that if we want to diagnose either  $\mathbf{U} \cdot \nabla q$ , or  $\mathbf{u} \cdot \overline{\nabla} Q$  individually, we then need to keep  
 916 the terms  $\Gamma_l J(\psi_l, \Psi_l)$  and  $\Gamma_l J(\Psi_l, \psi_l)$  because they only cancel in the sum.

## 917 **B5 Energy conservation**

918 The multi-scale model conserves energy in an asymptotic way (related to the scale separation  
 919 involved in the derivation). The fact that the model does not conserve energy is not an im-  
 920 plementation issue but is related to the derivation of the model. To illustrate this property, let us  
 921 consider an isolated eddy in the middle of the ocean. We can characterize this eddy by its kinetic  
 922 energy and its potential energy. If we move this eddy from one geographical location to another  
 923 without deforming it, we expect that its kinetic energy remains constant. On the other hand, its  
 924 potential energy is not conserved. Indeed, the potential energy of the eddy depends on its buoy-  
 925 ancy anomaly but also of the background stratification  $N^2$  which is a function of space. In the  
 926 QG formalism, the potential energy corresponds to the available potential energy and is defined  
 927 as a small perturbation of isopycnal surfaces around reference state. If an eddy moves from one  
 928 place to another, its potential energy will then vary because the reference stratification is a slow  
 929 function of space.

930 To do an energy budget, we multiply Eq. (8) by  $-\psi$  and integrate over the entire domain.  
 931 Let us consider only the advection of small-scale PV by the small-scale velocity

$$\begin{aligned}
 -\psi J(\psi, q) &= -\psi J(\psi, \nabla^2 \psi + \Gamma \psi) \\
 &= -\psi J(\psi, \nabla^2 \psi) - \psi J(\psi, \Gamma \psi)
 \end{aligned} \tag{B8}$$

932 The first term in the rhs is the usual kinetic energy conservation in QG, which does not pose any  
 933 problem here (thanks to the non-divergent definition of the velocity). However, if we integrate  
 934 the second term over the domain we have

$$\begin{aligned}
 \int_{\Omega} -\psi J(\psi, \Gamma\psi) &= \int_{\Omega} -\frac{1}{2} J(\psi^2, \Gamma\psi) \\
 &= \int_{\Omega} \frac{1}{2} \frac{f^2}{N^2} J(\partial_z \psi^2, \partial_z \psi) \\
 &= \int_{\Omega} \frac{1}{2} \frac{f^2}{N^2} J(\psi, (\partial_z \psi)^2) \\
 &= \int_{\Omega} \frac{1}{2} \frac{f^2}{N^2} J(\psi, b^2)
 \end{aligned}
 \tag{B9}$$

935 where we recall that we do not take derivative of the large scale variables (namely the stretch-  
 936 ing operator) and  $\Gamma = \partial_z(f^2/N^2 \partial_z(\cdot))$ .

937 The last term in the integral is formally equal to the advection of potential energy, but from  
 938 a numerical prospective, this integral is non zero as soon as  $f^2/N^2$  is non constant and so poten-  
 939 tial energy is not conserved. Again this property has a physical meaning (background stratifica-  
 940 tion varies in space) and is rooted in the definition of the model. This integral vanishes in the asymp-  
 941 totic limit of scale separation.

942 There are two conditions to have a “good” energy conservation:

- 943 • Eddies should remain small compared to the horizontal variations of  $f$  and  $N$
- 944 •  $f/N$  should remain small (which is why we imposed a minimum value on  $N$ )

945 As a side note, we remark that the numerical modeling community have focused a lot more  
 946 on numerical schemes that conserve kinetic energy (and enstrophy) but have not really looked  
 947 at potential energy conserving schemes with the notable exception of isopycnal models which  
 948 conserve both mass and thus potential energy.

## 949 **B6 Inversion of the elliptic equation**

950 We implemented a 3D solver to invert the elliptic equation (Eq. 4). We used a multigrid  
 951 solver in the horizontal and solved the tridiagonal system (for the vertical stretching term ) with  
 952 the Thomas algorithm a each relaxation step.